Evaporation from the Lunar Magma Ocean Was Not the Mechanism for Fractionation of the Moon's Moderately Volatile Elements

H. Tang and E. D. Young
Department of Earth, Planetary, and Space Sciences, UCLA, USA; haolantang@ucla.edu

Abstract

The cause of chemical depletion and isotopic fractionation of moderately volatile elements (MVEs) in the Moon is a long-standing problem. Here we examine MVE isotopic fractionation during Moon formation using potassium as a primary example. We show that the degree of isotopic fractionation due to evaporation of the lunar magma ocean (LMO) depended critically on the vapor pressure above the LMO. Based on our analysis of evaporation and escape of the resulting rock-vapor atmosphere, LMO evaporation alone could not have caused the observed MVE isotopic compositions. The combination of exposure of the liquid of the LMO to the surface for on the order of 10^2–10^3 yr, near-equilibrium evaporation at the melt surface, and hydrodynamic escape facilitated by proximity of the Earth leads to no resolvable isotope or elemental fractionation. This study provides a basis for the simplifying assumption that rock vapor immediately above a magma ocean will be in thermodynamic equilibrium with the melt at the surface of the planetary body even where hydrodynamic escape is operative.

Unified Astronomy Thesaurus concepts: Earth–Moon system (436); Isotope shifts (2069); Lunar evolution (952); The Moon (1692); Lunar science (972)

1. Introduction

The Moon has been widely thought to form from a giant impact between the proto-Earth and a planetary embryo impactor (e.g., Hartmann & Davis 1975; Cameron & Ward 1976; Canup & Asphaug 2001; Pahlevan & Stevenson 2007; Canup 2012; Ćuk & Stewart 2012). This giant impact is thought to have generated a silicate vapor-rich disk structure (e.g., Ward & Cameron 1978; Lock & Stewart 2017; Lock et al. 2018) from which the Moon later condensed. The giant-impact Moon formation event has been invoked to explain the chemical and physical characteristics of the Moon, including its mass, its small iron core, its volatile depletion, and its striking similarity to Earth in many elemental abundances and isotope ratios (e.g., O, W, Mg, Ti, and Si; Armytage et al. 2012; Zhang et al. 2012; Sedaghatpour et al. 2013; Kruijer et al. 2015; Touboul et al. 2015; Young et al. 2016). The explanation for the volatile depletion remains elusive, however. Indeed, some volatile-rich lunar pyroclastic glasses may indicate the presence of more volatile-rich reservoirs in the lunar interior, further complicating matters (Saal et al. 2013; Hauri et al. 2015; Day et al. 2017).

Isotope ratios of moderately volatile elements (MVEs, defined as elements with 50% condensation temperatures of 800 to ∼1290 K; Lodders 2003) are clues to the processes attending the giant impact and/or its immediate aftermath. Previous studies of MVE isotope ratios, including those for K, Zn, Cl, Ga, and Rb, have demonstrated that the Moon has distinctive isotope ratios of these elements compared to those of the Earth (Sharp et al. 2010; Paniello et al. 2012; Boyce et al. 2015; Wang & Jacobsen 2016; Kato & Moynier 2017; Pringle & Moynier 2017; Nie & Dauphas 2019; Wimpenny et al. 2019). For example, ^{41}K/^{39}K in lunar samples is higher than terrestrial values by ∼0.4‰ (δ^{41}K ∼ 0.4‰ where δ^{41}K = ([^{41}K/^{39}K]$_{sample}$/[^{41}K/^{39}K]$_{Earth}$ − 1) × 1000);

Wang & Jacobsen 2016). Various volatile-loss mechanisms have been proposed to explain these isotopic signatures (Day & Moynier 2014). Among these models is evaporation of the lunar magma ocean (LMO) and eventual escape from the transient atmosphere that results (e.g., Day & Moynier 2014).

In the case of K, the high δ^{41}K has been attributed to the Moon-forming giant impact event itself, in which the Moon incompletely condensed from a bulk silicate Earth (BSE) vapor at an ambient gas pressure greater than 10 bar (Wang & Jacobsen 2016). Similar shifts toward elevated relative abundances of the heavy isotopes have been observed in other lunar MVEs. High-precision Rb isotopic analyses of lunar samples indicate that the moon is generally depleted in Rb and has ^{87}Rb/^{85}Rb ratios greater than BSE by ∼+0.16‰ (Pringle & Moynier 2017; Nie & Dauphas 2019). Previous models suggest that this Rb isotopic value may reflect volatile loss in the precursor planetary bodies (Pringle & Moynier 2017) or result from near-saturated evaporation in the protolunar disk, due to gas viscosity associated with magnetor-otational instability (MRI; Nie & Dauphas 2019). In addition, despite different geochemical behaviors, Ga and Zn isotopic compositions also show a systematic enrichment in the heavier isotopes in lunar mare basalts, suggesting an extensive global-scale depletion event. The elements exhibiting heavy isotope enrichment share the characteristic that they exist primarily as monatomic species in the gas phase. Conversely, Cr and Sn are predicted to exist mainly as oxide species in the vapor phase on the basis of thermodynamic data (Sossi et al. 2019). Recent studies of the isotopic compositions of Cr and Sn in lunar samples show that these elements exhibit relatively light isotopic compositions, consistent with equilibrium isotope partitioning between oxide vapor and silicate melt (Sossi et al. 2018; Wang et al. 2019). The fractionation of MVEs should have occurred shortly before or during crystallization of the near-surface molten rock comprising the LMO that existed immediately after coalescence of the Moon (Day & Moynier 2014; Kato et al. 2015; Dhaliwal et al. 2018).

The prevalence of MVE isotope fractionation eliminates partial condensation as the sole source of depletions of these elements. Condensation at relevant temperatures does not lead to heavy isotope enrichment (e.g., Simon & DePaolo 2010; Simon et al. 2017). Here we investigate evaporation from the surface of the LMO and escape from the rock-vapor atmosphere produced by evaporation as a potential mechanism for causing the observed enrichments in heavy isotopes of lunar MVEs. The formation of a magma ocean subsequent to the accretion of the Moon almost certainly occurred, making the events investigated here inevitable over at least a brief time interval. In this analysis we assume that the Moon formed essentially dry because of partial condensation, and as a consequence, MVEs, not water, dominated the atmosphere above the LMO (Lock et al. 2018). We use the fractionation of K isotopes as a test case. Our results show that MVE heavy isotope enrichments cannot be attributed to LMO evaporation alone. Instead, isotopic equilibrium at high temperatures should have occurred between vapor and melt just above the surface of the magma ocean. Isotopic equilibration at such high temperatures cannot explain the observed fractionation of K isotopes for lunar samples. In addition, we find that atmospheric escape also cannot have fractionated the lunar MVEs at conditions relevant for the LMO.

In what follows we first describe the isotopic effects of evaporation considering the feedback between the overlying vapor and the silicate melt (Section 2). We then consider the formation of a steady-state rock-vapor atmosphere formed by the balance between evaporation at the transiently molten surface of the LMO and atmospheric escape (Section 3). The efficacy of escape in affecting the isotopic composition of the Moon is evaluated in Section 4. The implications of these results are discussed in Section 5, and we summarize our conclusions in Section 6.

2. Isotopic Fractionation between Vapor and Melt during Evaporation

The depletion of MVEs in the Moon points toward volatility as the controlling mechanism. Evaporation and condensation are the operative processes where elements and isotopes are separated (fractionated) by volatility. Any model for the isotopic effects of volatilization must include the interaction between these two opposing phenomena. In the limit of equal rates of evaporation and condensation, an isotopic equilibrium obtains between vapor and melt. The equilibrium isotope fractionation factor between vapor and melt is expressed as the ratio of the melt isotope ratio to that of the vapor at equilibrium, or $(n'_{i,\text{melt}}/n_{i,\text{melt}})/(n'_{i,\text{vapor}}/n_{i,\text{vapor}})$, where n_i refers to the number density of species i for the indicated phase and the prime represents the heavy isotope of i. The law of mass action requires that $\alpha_{i,\text{eq}}$ is related to the condensation and free evaporation fractionation factors such that

$$\alpha_{i,\text{eq}} = \frac{\alpha_{i,\text{cond}}}{\alpha_{i,\text{evap}}}. \tag{1}$$

Here the free evaporation isotope fractionation factor ($\alpha_{i,\text{evap}}$) can be measured directly in the laboratory and is defined as the ratio of the isotope ratios of the species i in the evaporating gas to that in the melt, or $(n'_{i,\text{vapor}}/n_{i,\text{vapor}})/(n'_{i,\text{melt}}/n_{i,\text{melt}})$, where there is no return flux from gas to melt. In contrast, laboratory measurements of the condensation fractionation factors ($\alpha_{i,\text{cond}}$) are challenging, but they can be constrained by the more easily

measured or calculated equilibrium fractionation factors together with the evaporation fractionation factors because $\alpha_{i,\text{cond}} = \alpha_{i,\text{eq}} \, \alpha_{i,\text{evap}}$. Equation (1) accounts for different zero-point energies of light and heavy isotopes that determine the equilibrium partitioning of the isotopes between phases (e.g., liquid and gas) and the kinetics of bond rupture and formation. It does not include fractionation related to transport of the gas phase to and from the surface of the evaporating melt. The zero-point energy effect of condensation generally favors the heavy isotope in the melt phase for monoatomic species like MVEs here, while gas transport favors delivery of the light isotopic species in the gas to the melt surface. In order to account for these opposing effects, one must include both transport and the energetics of condensation. This is done by casting the problem of isotope fractionation between vapor and melt in terms of vapor saturation (e.g., Simon & DePaolo 2010; Simon et al. 2017).

In what follows we make use of the saturation index $S_i = P_i/P_{i,\text{eq}}$, in which i denotes the species of interest and P_i and $P_{i,\text{eq}}$ are the partial pressure of i and the equilibrium vapor pressure of i, respectively. Condensation dominates over evaporation where $S_i > 1$, evaporation dominates where $S_i < 1$, and $S_i = 1$ denotes vapor–melt equilibrium where the rates of evaporation and condensation are equal. We will mainly focus on the evaporation isotopic fractionation factor when $S_i \leqslant 1$ given that it is well documented that partial condensation where $S_i > 1$ will result in isotopically light condensates compared to the isotopic composition of the vapor (e.g., Simon & DePaolo 2010). Thus, the heavy isotopic composition of MVEs cannot be attributed to partial condensation during the Moon's accretion.

2.1. Fractionation where $S_i = 1$

Where $S = 1$, isotopic equilibrium between melt and vapor obtains. In the specific case of potassium isotopes, the melt–vapor equilibrium fractionation factor for $^{41}K/^{39}K$, $\alpha_{K,\text{eq}} = (n_{41K,\text{melt}}/n_{39K,\text{melt}})/(n_{41K,\text{vapor}}/n_{39K,\text{vapor}})$, can be estimated using K-feldspar as the condensed phase. The $KAlSi_3O_8$–vapor fractionation factor as a function of temperature is obtained from the ratio of reduced partition function ratios (β factors) for $^{41}K/^{39}K$ in microcline and in the vapor. Potassium is coordinated by eight oxygen atoms in K-feldspar, and bond distances range from 2.83 to 3.23 Å. Based on these parameters, the model developed in Young et al. (2015) yields for microcline

$$1000 \ln \beta_{\text{microcline}} = 0.1537 \frac{10^6}{T^2}. \tag{2}$$

Our calculation is consistent with the calculation done by Zeng et al. (2019). Since K in the vapor phase is present as the atomic species, no vibrational energy is present in the gas-phase K and $\beta_{\text{gas}} = 1$. Therefore, $\alpha_{K,\text{eq}}(KAlSi_3O_8/\text{vapor}) = \beta_{\text{microcline}}/\beta_{\text{gas}} = \beta_{\text{microcline}}$, and the equilibrium melt–vapor isotope fractionation factor is given by Equation (2) such that $1000 \ln \alpha_{K,\text{eq}} = 0.1537(10^6/T^2)$. Although we use microcline as an example K-bearing phase, theoretical β factors for $^{41}K/^{39}K$ for different feldspar phases at $T \geqslant 1800$ K (e.g., Li et al. 2019; Wang et al. 2019; Zeng et al. 2019) give qualitatively similar results in that

none would yield resolvable equilibrium melt–vapor isotope fractionation factors at relevant temperatures.

2.2. Fractionation where $S_i < 1$

Values of $S_i < 1$ signify evaporation. Rates of evaporation depend on the difference between the equilibrium (saturation) vapor pressure and the extant vapor pressure surrounding the evaporating melt. The evaporative flux of the species of interest i from a melt is given by the Hertz–Knudsen equation:

$$J_{i,\text{net}} = \frac{\gamma_i(P_{i,\text{eq}} - P_i)}{\sqrt{2\pi m_i RT}} \quad (3)$$

where $P_{i,\text{eq}}$ is the equilibrium vapor pressure of gas species i, P_i denotes the actual vapor pressure, m_i represents the molecular mass of species i, γ_i is the evaporation coefficient for i, R is the ideal gas constant, T is temperature, and $J_{i,\text{net}}$ denotes the net evaporative flux of gas species i. The evaporation coefficient γ_i reflects the efficiency of species i crossing the melt–vapor interface compared to the maximum that could cross. Values for γ_i are not generally amenable to estimation by first principles and instead are determined empirically. The net evaporative flux of species i, $J_{i,\text{net}}$, is the difference between the "free" evaporative flux that is proportional to the equilibrium vapor pressure ($P_{i,\text{eq}}$) only and the return flux associated with the actual extant pressure (P_i). The ratio of net evaporation to free evaporation is $J_{i,\text{net}}/J_{i,\text{evap}} = 1/(1 + J_{i,\text{return}}/J_{i,\text{net}})$, and this results in (Carslaw & Jaeger 1959; Richter et al. 2002; Young et al. 2019)

$$J_{i,\text{net}} = \frac{J_{i,\text{evap}}}{1 + \frac{\gamma_i RT}{\sqrt{2\pi m_i RT}}\frac{s}{D_i}[1 - e^\xi \,\text{erfc}\,(\sqrt{\xi})]} \quad (4)$$

in which s is the radius of the evaporating body, D_i is the gas-phase diffusion coefficient for the species i, and $\xi = tD_i/s^2$ is the dimensionless elapsed time from the beginning of evaporation. For the ambient total pressure P, the gas-phase diffusion coefficient of species i is $D_i = (2/(3\sqrt{\pi}))$ $(1/(\sigma P\sqrt{\mu_i}))(k_B T)^{3/2}$, where σ is the collisional cross section and μ_i is the reduced mass for species i in the vapor. Equation (4) reduces to the free evaporation flux where the return flux is zero, as seen by considering the limits where $P \to 0$ and $D_i \to \infty$, resulting in

$$S_i = \frac{P_i}{P_{i,\text{eq}}} = 1 - \frac{1}{1 + \frac{\gamma_i RT}{\sqrt{2\pi m_i RT}}\frac{s}{D_i}[1 - e^\xi \,\text{erfc}\,(\sqrt{\xi})]} = 0, \quad (5)$$

and by inspection of Equations (4) and (5), we have

$$J_{i,\text{net}} = J_{i,\text{evap}}. \quad (6)$$

Importantly for this study, Equation (4) can be applied to calculate evaporative net fluxes of light and heavy isotopes from a body with finite return fluxes. Given $\alpha_{\text{cond}} = \alpha_{\text{eq}}\alpha_{\text{evap}}$, the return flux of the heavy isotope of species i can be expressed as $J'^*_{i,\text{return}} = \alpha_{\text{eq}}\alpha_{\text{evap}}J'_{i,\text{return}}$, where $J'^*_{i,\text{return}}$ denotes the return flux of the heavy isotope ($J'_{i,\text{return}}$) accounting for the bond energy effects of condensation α_{cond} (see Equation (1)). The ratio of net fluxes for two isotopes of the same element

evaporating from the melt, together with the ratio of the isotopes in the evaporating melt, $n'_{i,\text{melt}}/n_{i,\text{melt}}$, yields the net evaporation isotope fractionation factor $\alpha_{i,\text{net}}$ for species i:

$$\alpha_{i,\text{net}} = \frac{\left(\frac{J'^*_{i,\text{net}}}{J_{i,\text{net}}}\right)}{\left(\frac{n'_{i,\text{melt}}}{n_{i,\text{melt}}}\right)}$$

$$= \alpha_{i,\text{evap}}\frac{1 + \frac{\gamma_i RT}{\sqrt{2\pi m_i RT}}\frac{s}{D_i}[1 - e^\xi \,\text{erfc}\,(\sqrt{\xi})]}{1 + \frac{\alpha_{i,\text{eq}}\alpha_{i,\text{evap}}\gamma_i RT}{\sqrt{2\pi m'_i RT}}\frac{s}{D'_i}[1 - e^\xi \,\text{erfc}\,(\sqrt{\xi})]}, \quad (7)$$

where the prime superscript signifies the heavy isotope (Equation (7) is derived in Appendix A). In the limit of relatively long timescales where $1 - e^\xi \,\text{erfc}\,(\sqrt{\xi}) \to 1$ and with sufficiently high return fluxes, $S_i \to 1$ and $\alpha_{i,\text{net}} \to 1/\alpha_{i,\text{eq}}$, implying equilibrium isotopic fractionation between gas and melt. Note that we use collisional reduced masses μ_i and μ'_i to replace molecular masses in Equations (4)–(7) in what follows because the collision partners affect the transport of species of interest in the gas phase.

2.3. Potassium Isotopic Fractionation during Evaporation from the LMO

One mechanism for enriching the bulk Moon in heavy isotopes of K is evaporation from a magma ocean exposed to the surface. The size of the evaporating body and the enveloping background vapor pressure are significant factors that control the evaporation behavior of molten rock (see Equation (7)). For example, compared with the background pressure of ~1 bar (10^5 Pa) required to achieve saturation for millimeter-sized molten spheres that solidified to form chondrules in chondrite meteorites, the background vapor pressures required for saturation for large planetary-scale bodies are much lower. Figure 1(A) shows the variation of the ratio of net evaporative flux to free evaporation flux, $J_{\text{net}}/J_{\text{evap}}$, for ^{39}K as a function of time and the radius of the evaporating body for a total ambient vapor pressure of 2×10^{-7} bar (2×10^{-2} Pa) at 1800 K. The evaporation IDL+Fortran code described previously by Young et al. (2019) was used to calculate the K free evaporation fluxes shown here (see Section 4.1). Results for evaporating bodies with radii of 500, 1000, and 1700 km (Moon-size) are shown for comparison. Additionally, two evaporation coefficients are shown for potassium as determined for free evaporation into a vacuum ($\gamma_K = 0.1$) and evaporation into an ambient gas with 9×10^{-5} bar H_2 ($\gamma_K = 0.017$; Fedkin et al. 2006) as an illustration of the sensitivity to α_K. Although these evaporation coefficients were determined for chondritic compositions rather than for basaltic compositions, the calculations illustrate that $J_{i,\text{net}}/J_{i,\text{evap}} \ll 1$, signifying that the K in this melt–vapor system is approaching saturation ($J_{i,\text{net}}/J_{i,\text{evap}} = 0$ at saturation) under these conditions. Also, $J_{i,\text{net}}/J_{i,\text{evap}}$ decreases with increasing radius after ~10 yr for these conditions, showing that larger bodies come closer to saturation, all else equal. In general, the K vapor achieves 99% saturation after just 400,000 s (~4 days) for bodies on the order of >500 km in radius.

Given equilibrium and free evaporation fractionation factors, the net fractionation factor can be calculated as a function of ambient background pressure using Equation (7). Figure 1(B) shows α_{net} for K and Rb as a function of pressure for evaporation from a Moon-sized body at 1800 K and relatively long timescale $1 - e^\xi \,\text{erfc}\,(\sqrt{\xi}) \to 1$ in Equation (7). At

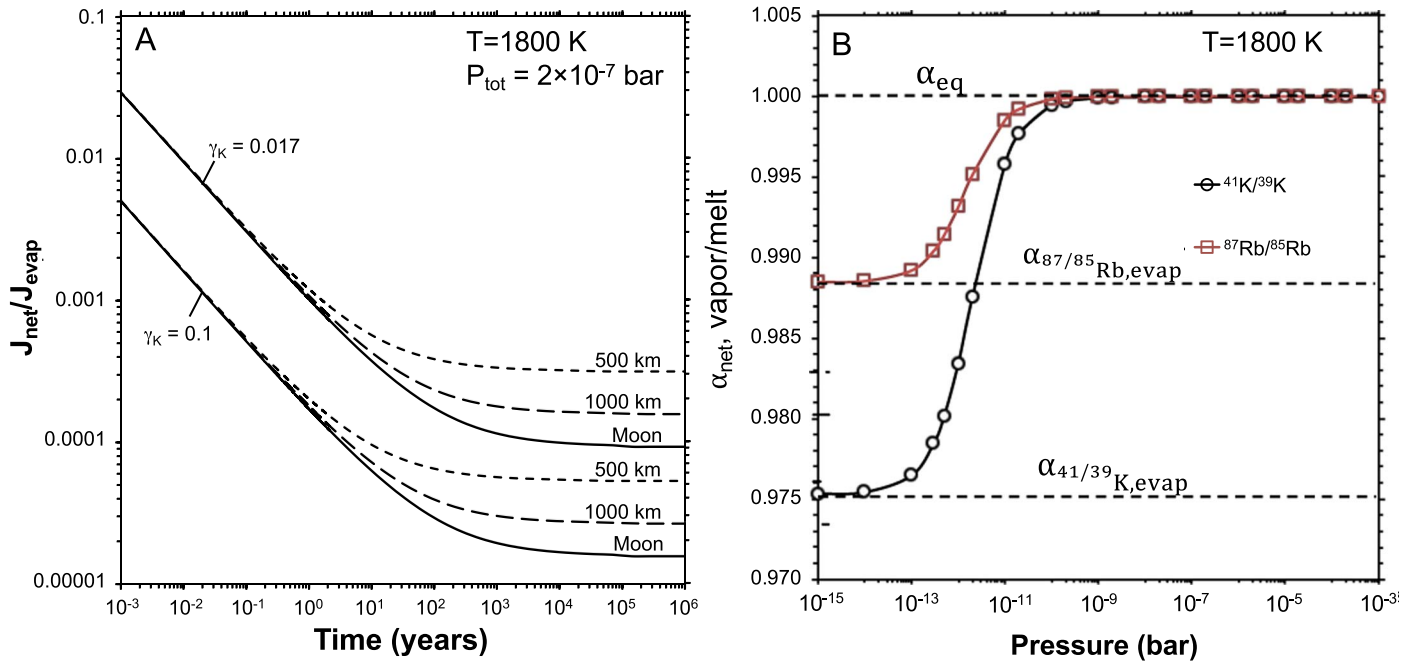**Figure 1.** Effects of ambient pressure on net evaporative flux and net isotope fractionation factors. (A) J_{net}/J_{evap} for K as a function of time and size of the evaporating body at 1800 K and a total pressure of 2×10^{-7} bar. J_{evap} is calculated using the evaporation code described by Young et al. (2019) and in the text. In this plot, $J_{net}/J_{evap} = 1$ corresponds to free evaporation and $J_{net}/J_{evap} = 0$ corresponds to saturation. The decreasing ratio of net evaporative flux to free evaporative flux with increasing evaporation duration indicates that evaporation on the bodies with radii of 500, 1000, and 1700 km (about the size of the Moon) leads to a close approach to saturation. The curves for different evaporation coefficients determined in previous experiments by Fedkin et al. (2006) are shown. (B) Net isotope fractionation factors for K and Rb for a Moon-sized body as a function of pressure based on Equation (7) and a temperature of 1800 K. Fractionation factors for K and Rb are asymptotic to equilibrium at pressures greater than 10^{-9} bar (10^{-4} Pa). The α_{evap} values for both K and Rb are based on the square root of the inverse mass ratios of their isotopes. The α_{eq} value for $^{41}K/^{39}K$ is from Equation (2) and that for $^{87}Rb/^{85}Rb$ is estimated based on the theoretical calculation by Zeng et al. (2019). The data files for these plots (ds01 and ds02) can be accessed at doi:10.7910/DVN/LRIMT8.

1800 K with increasing background pressure, the net evaporation fractionation factors for $^{41}K/^{39}K$ and $^{87}Rb/^{85}Rb$ ascend rapidly from the value of free evaporation at the lowest pressures to equilibrium where $P > 10^{-9}$ bar (10^{-4} Pa). K and Rb in the vapor are effectively saturated at these pressures, due to the efficacious return flux with $S_K \sim S_{Rb} \sim 1.00$.

The results summarized in Figure 1 illustrate that the crucial parameter that controlled MVE isotope fractionation factors was the pressure of the rock-vapor atmosphere above the LMO. That pressure can be estimated based on the structure of the atmosphere.

3. The Rock-vapor Atmosphere

The pressures of gas above the LMO, and thus the isotopic effects of evaporation, will have been controlled by the balance between the rate of evaporation and rate of vapor escape. These rates conspire to produce a steady-state rock-vapor atmosphere above the LMO while the melt is exposed to space (Young et al. 2019). Here we calculate the structure of this atmosphere as a function of the different atmospheric escape mechanisms. The rate of escape depends on intrinsic factors (temperature, density structure) as well as on extrinsic forces (Earth–Moon distance).

3.1. Vapor Composition Due to Magma Ocean Evaporation

The total and partial pressures of the rock vapor atmosphere resulting from evaporation of a basaltic melt determine the isotopic effects of magma ocean evaporation. The evaporative fluxes emanating from CaO–MgO–Al$_2$O$_3$–SiO$_2$ (CMAS) melts

as well as chondritic melts have been well studied from both theory and experiments (e.g., Davis et al. 1990; Floss et al. 1996; Young et al. 1998; Grossman et al. 2000; Alexander 2001; Richter et al. 2002, 2007; Richter 2004; Fedkin et al. 2006; Shahar & Young 2007; Grossman et al. 2008; Knight et al. 2009). The equilibrium vapor pressures driving free evaporation have been previously parameterized for CMAS melts (Grossman et al. 2000; Richter et al. 2002; Shahar & Young 2007). Here we modified the IDL+Fortran code described by Young et al. (1998, 2019) and Shahar & Young (2007) to expand the applicable composition space from the reference CMAS system to one that includes Fe, Na, and K. We used the chemical thermodynamics expressions for the partial pressures of Fe, Na, and K in equilibrium with silicate melt oxide components FeO, Na$_2$O, and K$_2$O. Substitution of these thermodynamically defined equilibrium vapor pressures into Equation (3) leads to a general expression for the free evaporation flux of metal M given the oxide melt component MO_x (x is the stoichiometric coefficient for the oxygen):

$$J_M = x_{MO_x}^{melt} \gamma_{MO_x}^{melt} \frac{\exp(-\Delta\hat{G}_{MO_x \to M+1/2x\,O_2}^{\circ} / (RT))}{\sqrt{2\pi RT\, m_M}} P_{O_2}^{-(1/2)x},$$

(8)

where $\Delta\hat{G}_i^o$ is the molar free energy of reaction i at standard state, $x_{MO_x}^{melt}$ and $\gamma_{MO_x}^{melt}$ are the mole fraction and activity coefficient for oxide MO_x in the evaporating melt, and m_M is the molar mass of metal species M. The ratio of the flux defined by Equation (8) to the analogous expression for MgO allows us

to take full advantage of the experimental calibration for evaporation of Mg. The general expression for the ratio of the free evaporative flux of metal M to that for Mg is

$$\frac{J_M}{J_{\text{Mg}}} = \frac{x_{MO_x}^{\text{melt}} \gamma_{MO_x}^{\text{melt}}}{x_{\text{MgO}}^{\text{melt}} \gamma_{\text{MgO}}^{\text{melt}}} \sqrt{\frac{m_{\text{Mg}}}{m_M}}$$

$$\times \exp\left(\frac{\Delta \hat{G}^{\circ}_{\text{MgO}\rightarrow\text{Mg}+1/2\text{O}_2} - \Delta \hat{G}^{\circ}_{MO_x\rightarrow M+1/2x\,\text{O}_2}}{RT}\right) P_{\text{O}_2}^{(1/2)(1-x)}$$

(9)

where the dependence on the partial pressure of O_2 results in a modest pressure dependence on the flux of alkalis relative to Mg. The higher the P_{O_2}, the greater is the ratio $J_{\text{Na}}/J_{\text{Mg}}$, for example. This is understood as the result of the lower mole fraction of O_2 from evaporation of $NaO_{1/2}$ than from evaporation of MgO. Here the partial pressure of O_2 is calculated from the mole fraction of O_2 in the gas dictated by the evaporative fluxes multiplied by the total pressure. Evaporation into a background pressure of $\sim 10^{-8}$ bar at 1800 K with 30% O_2 in the evaporated gas results in $P_{O_2} \sim 0$ on the ΔIW oxygen fugacity scale [ΔIW = log$f$O$_2$–log$f$O$_2$ (iron-wüstite buffer curve)]. The expanded CMAS-based models simulate the evaporative fluxes of K, Na, Fe, Mg, SiO, AlO, and CaO from the melt (hereafter cited as the KNFCMAS model). In order to evaluate Equation (9), we use the NIST thermodynamic database and activity coefficients for $NaO_{1/2}$ and $KO_{1/2}$ during evaporation from Sossi et al. (2019) and activity coefficients for FeO and MgO given by Wood & Wade (2013) and Schaefer & Fegley (2004). The melt composition is taken to be the lunar primitive upper mantle bulk silicate Moon (LPUM): 38.53 wt% MgO, 44.24 wt% SiO_2, 10.0 wt% FeO, 2.96 wt% CaO, 4.16 wt% Al_2O_3, 0.11 wt% Na_2O, and $\sim$50 ppm K (Longhi 2006). Based on this relatively Na-depleted initial bulk composition, Na is the dominant species in the vapor for melt evaporation temperatures from the solidus to $\leqslant$2000 K; evaporation of the LPUM melt over this temperature range generates Na vapor with about 6%–7% K vapor. The predominance of Na is consistent with previous evaporation experiments using chondritic compositions (Yu et al. 2003; Fedkin et al. 2006). Here we confine our calculations to 1800 K $\leqslant T \leqslant$ 2000 K, where the silicate is largely molten and alkali elements predominate in the vapor. At temperatures >2000 K for similarly alkali-depleted silicate melts, SiO and Mg become important constituents of the rock-vapor atmosphere. However, thermal models of the surface magma ocean suggest that such high temperatures at the surface would be very short lived (see Appendix B, Figure B1).

3.2. Structure of the Rock-vapor Atmosphere

3.2.1. Thermal Effect from the Post–Giant Impact Earth

The possibility that the Moon was tidally locked to the Earth as early as <1 yr after its formation raises the prospect of disparate near- and far-side temperature regimes that are due to radiation from the post-impact Earth (Roy et al. 2014). Based on this possibility, Saxena et al. (2017) simulated the early lunar rock-vapor atmosphere considering the effects of Earth shine. They considered that an effective radiation temperature for the Earth of 2300–2500 K could have caused large near-side versus far-side variations in surface temperature on the

Moon, resulting in evaporation of MVEs on the near side and condensation on the far side. Lateral winds would have facilitated the transfer of the MVEs from the near side to the far side. The underlying assumption in this scenario is that the atmosphere of the post–giant impact Earth was optically thin within hundreds of years after the giant impact. Their lunar rock-vapor atmosphere pressures were assumed to be those prescribed by thermodynamic equilibrium vapor pressures above the LMO as calculated using the MAGMA code (Schaefer & Fegley 2004).

In the model presented here, we start with a different initial condition in which the Earth is shrouded in an optically thick atmosphere dominated by volatile species (e.g., H_2O, CO_2). Outgassing of hundreds of bars worth of volatiles would occur rapidly (on the order of years) for a molten post–giant impact Earth that had a rapidly convecting magma ocean (Elkins-Tanton 2008). Zahnle et al. (2015) showed that the effective temperature for Earth surrounded by such an atmosphere, $T_{E\text{ff},\oplus}$, would have been $\leqslant$500 K. Roy et al. (2014) calculated the radiative equilibrium temperature for the near side of the Moon from the contributions of the Sun and Earth using $T_{\text{Eq,near side}} = [T_{\odot}^4 R_{\odot}^2/(4a_{\odot}^2) + T_{E\text{ff},\oplus}^4 R_{\oplus}^2/(2a_{\text{Earth}-\text{Moon}}^2)]^{1/4}$ where $a_{\odot}$ is the Moon–Sun distance, $a_{\text{Earth}-\text{Moon}}$ is the Earth–Moon distance, and $R_{\odot}$ is the radius of the Sun. Accordingly, for the Moon accreted at Earth's Roche limit ($\sim 3R_{\oplus}$) or beyond, the equilibrium temperature imposed on the Moon by radiation from the postcollisional Earth should have been $\leqslant 1/2T_{E\text{ff},\oplus}$, or $\leqslant$250 K for our initial condition of an optically thick Earth atmosphere. Therefore, for a post–giant impact Earth with a thick atmosphere, the thermal effects of the radiating Earth were comparable to those of the Sun, and both were negligible compared with the heat radiated from the LMO. For these reasons, our calculations assume that there is no toroidal variation in thermal regime affecting the LMO or the lunar rock-vapor atmosphere.

Our rock-vapor atmosphere is considerably less dense than that considered by Saxena et al. because we do not assume a priori that the vapor pressure throughout the atmosphere is in thermodynamic equilibrium with molten rock. Rather, we consider the radial pressure profile of the rock-vapor atmosphere as the result of a balance between evaporation from the LMO at the surface and atmospheric loss rates far from the surface, as described in the following sections.

3.2.2. Alkali Vapor Atmosphere: Dry or Wet?

Conduction from the hot magma surface will have heated the bottom of the rock-vapor atmosphere, triggering a radial temperature gradient and convection above the LMO even in an optically thin atmosphere (Pierrehumbert 2010). In general, the rock-vapor atmosphere above the LMO will have had three distinct layers on the basis of pressure and temperature structure, including a convective layer (troposphere) at the base, a radiative layer (stratosphere), and an escape layer beyond which vapor escapes to space. In addition, the atmosphere can be described as comprising two layers based on the degree of mixing. In the homosphere, wave breaking leads to eddy diffusion that can mix the atmosphere effectively even above the convection layer. The effective eddy diffusivity k_{eddy} and the molecular diffusivity D both increase with altitude as pressure decreases (Yamanaka 1995), but at relatively low pressures, the capacity to sustain wave propagation eventually gives way to purely molecular diffusive transport. The region above this homopause is referred to as the heterosphere because it is no longer well mixed, the consequence of differential

gravitational settling according to molecular weight. In the case of Earth, the homopause occurs at an altitude of roughly 100 km (Catling 2015).

The structure of the rock-vapor atmosphere is determined by the steady-state pressure when the surface-integrated evaporative flux is equal to the surface-integrated escape flux. Low escape fluxes relative to evaporative fluxes will yield relatively high steady-state pressures directly above the LMO. At sufficiently high vapor pressures, alkali condensates could form in the troposphere as partial pressures approach saturation of Na and K. In this case, the opacity of the vapor–condensate mixture would be enhanced by liquid droplets, resulting in an optically thick atmosphere with temperatures following a wet adiabat. An optically thick atmosphere would control the cooling of the LMO, replacing radiation from the magma ocean surface as the primary governor on LMO cooling (De Pater & Lissauer 2006). In contrast, an evaporative flux balanced by a relatively high escape flux would lead to low steady-state pressures, in which Na and K are undersaturated. The low pressure combined with the low opacity of alkali vapor (Freedman et al. 2008) would result in an optically thin atmosphere. In this circumstance, temperatures in the troposphere would follow a dry adiabat, and cooling of the LMO is controlled primarily by the effective temperature at the surface of the magma ocean.

The saturation state of the Na-dominated rock-vapor atmosphere can be investigated using the equilibrium between vapor and liquid in the Na–O system:

$$1/2 Na_2O^{liquid} \rightleftharpoons Na^{gas} + 1/4 O_2^{gas}. \tag{10}$$
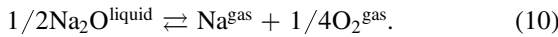
Here the liquid refers to droplets of Na_2O that might condense from the vapor phase. In the convective layer of the rock-vapor atmosphere above the magma ocean, temperatures are asymptotic to an isentropic adiabat. In the stratosphere portion of the rock-vapor atmosphere, above the convection layer, the vapor is essentially isothermal (Young et al. 2019). The conditions leading to different saturation states are therefore controlled by the profile of the atmosphere traced in P versus T and P versus S space (S = entropy here, not to be confused with saturation).

Where temperature and pressure are the state variables (e.g., for the upper atmosphere), the Na–O vapor–liquid system at equilibrium can be described by minimizing Gibbs free energy, resulting in the expression

$$0 = \Delta \hat{G}^{\circ}_{NaO_{1/2} \to Na + 1/4 O_2} + RT \ln(P_{Na}/1 \text{ bar})$$
$$+ 1/4 RT \ln(P_{O_2}/1\text{bar}) - RT \ln(a^{liquid}_{NaO_{1/2}}) \tag{11}$$

where the molar free energy refers to the standard state of 1 bar (10^5 Pa) and pure $NaO_{1/2}$ liquid. Under the conditions considered here, the activity for $NaO_{1/2}$, $a^{liquid}_{NaO_{1/2}}$, is unity (i.e., the condensate is pure Na oxide). Equation (11) provides the P versus T relationship between melt and vapor in the Na-dominated atmosphere.

Where entropy and pressure are the state variables (as in the adiabatic convective layer of the atmosphere), the Na–O vapor–liquid system at equilibrium is described by minimizing the enthalpy of the system. The resulting conjugate to the P versus T space is the P versus S space obtained from

$$0 = dH^{system} = TdS^{system} + VdP^{system}. \tag{12}$$

The relationships between S and P for the liquid and gas phases, dS/dP, are obtained from Maxwell's relations, from which we have

$$-\left(\frac{dP}{dS}\right)_V = \left(\frac{dT}{dV}\right)_S = \frac{1}{\alpha_v V} \tag{13}$$

where α_V is thermal expansivity. In the case of an ideal gas (our atmosphere), $\alpha_V = 1/T$, and our Equation (13) is then

$$-\left(\frac{dP}{dS}\right)_V = \frac{P}{nR} \tag{14}$$

where n is the moles of gas. Integration of (14) yields the expression for the entropy of the gas phase as a function of pressure:

$$\hat{S}^{gas} = \hat{S}^{o,gas} - R \ln(P/P^o) \tag{15}$$

where the entropies are expressed as molar quantities and the superscript ^{o} signifies the standard-state condition taken as the pure phase at 1 bar and the temperature of interest. The analogous expression for the liquid phase, $dS = -(\alpha_v V)dP$, has a negligible pressure effect on the liquid entropy, due to small values for the liquid expansivity.

The NIST thermodynamic database was used to evaluate Equations (11) and (15) with temperature-dependent molar Gibbs free energies and entropies, resulting in the conjugate P versus T and P versus S diagrams in Figure 2 for the Na–O system. The two diagrams illustrate the phase changes expected for the Na-rich atmosphere as a function of pressure, and thus altitude. Two schematic profiles are shown for an initially undersaturated Na-rich atmosphere produced by evaporation of the magma ocean under conditions broadly applicable to the LMO. One profile corresponds to a more-dense, optically thick atmosphere occurring at higher pressures at the base of the atmosphere, and the other corresponds to a less-dense, optically thin atmosphere with lower initial pressure.

In the case of the more-dense atmosphere, as pressure decreases upward above the magma ocean surface, the gas follows the isentropic adiabat labeled "1" in Figures 2(A) and (B). As temperature decreases along the adiabat with altitude, the gas phase becomes saturated and Na oxide "rain" is expected to form. In P–T space, the system is constrained to follow the two-phase boundary, while it traces a vertical profile in P–S space (labeled "2" in Figure 2). The fraction of Na that precipitates as liquid is indicated by applying the lever rule to the profile in P–S space, in which the mass fractions of vapor and liquid can be estimated based on the inverse proportions of the horizontal distances between the isentropic profile and phase boundaries (d_1 and d_2 in Figure 2(B); Stolper & Asimow 2007). At the high temperatures that obtain for the vapor above the LMO (see below), the isentropic gas (path "2a" in Figure 2(B)) is much closer to the gas P–S curve than it is to the liquid P–S curve, showing that even at the relatively high ground-level pressures chosen for this illustration (~1 mbar), most of the Na will remain in the vapor phase. Nonetheless, under these conditions, some Na oxide "rain" is expected. If the low-entropy Na oxide rain is removed from the parcel of atmosphere, the path of the gas will resemble "2b" in Figure 2(B), following the high-entropy gas-phase P–S curve. The presence of Na_2O condensates could dramatically increase the atmosphere optical depth (τ) because of the high Rosseland mean opacity of the condensed phase (e.g., Semenov et al. 2003), potentially resulting in a lower "skin temperature." Above the top
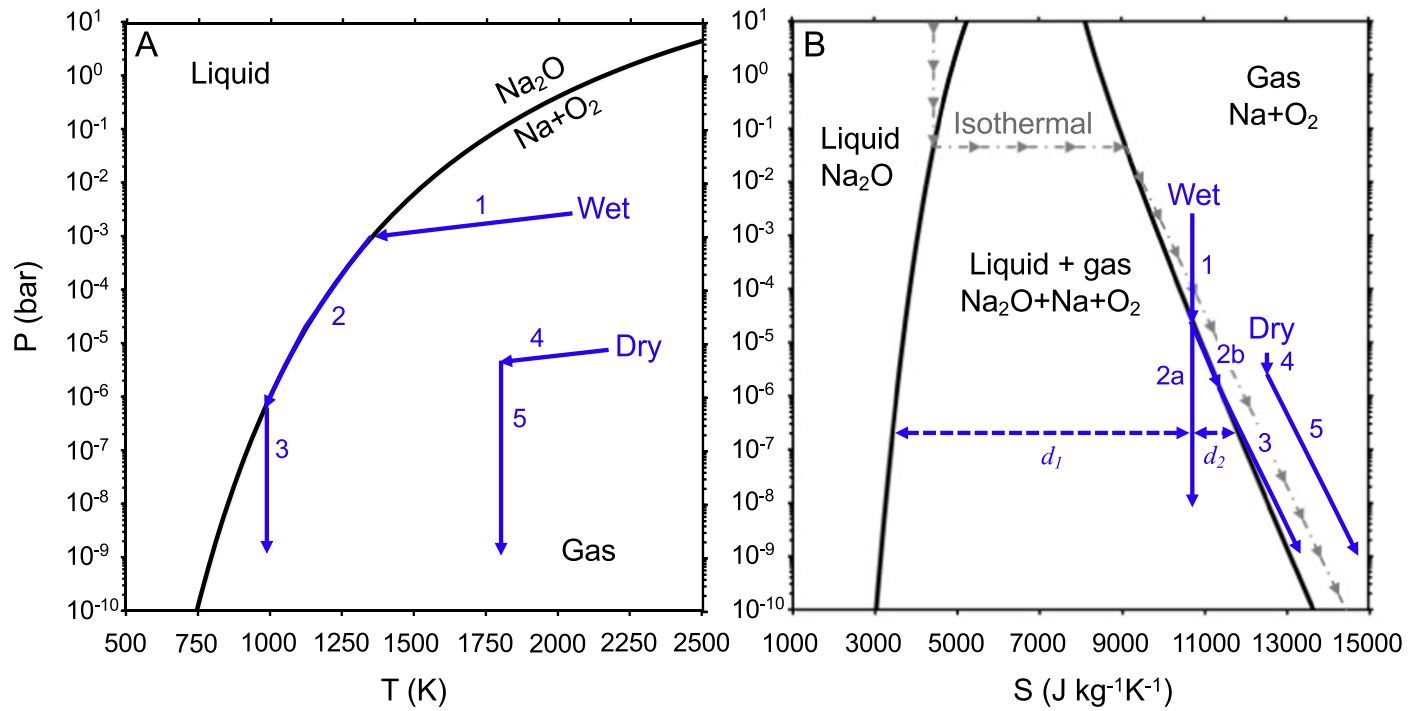
Figure 2. Schematic pressure–temperature (A) and pressure–entropy (B) profiles from the base of a Na-dominated rock-vapor atmosphere to the top of the atmosphere for the optically thick and optically thin cases. In both figures, arrows 1–3 illustrate the changes in P, T, and S of the atmosphere with greater altitude for the optically thick case in which alkali precipitation occurs at high altitudes. Arrows 4–5 illustrate the profile for the optically thin case with undersaturated Na vapor throughout the entire atmosphere. The shift from the cooling portions of the profiles to the isothermal portions of the profiles represents passage from the convective layer to the isothermal stratosphere above the tropopause with altitude. The gray dashed–dotted line in (B) represents an example of an isothermal path in the Na–O system. Two possible P–S paths are shown for the coexistence of Na_2O melt and $Na + O_2$ gas. Diagrams were calculated using thermodynamic data from the NIST database. The data file for Figure 2 (ds03) can be accessed at doi:10.7910/DVN/LRIMT8.

of the convecting troposphere, the profile of the gas is no longer adiabatic. Instead, pressures are low enough that the atmosphere is isothermal (e.g., path "3" in Figures 2(A) and (B)) or nearly so. At these elevations, Na oxide is entirely in the vapor phase once again. We note that an alkali-rich atmosphere produced at the high temperatures that existed above the LMO would collapse if condensation resulted in optical depths sufficient to lower the skin temperature below ~700 K (no vapor would be stable, Figure 2); there are limits to how optically thick a viable alkali-rich rock-vapor atmosphere can be.

In the case of a less-dense atmosphere, as pressure decreases upward, the gas follows the dry adiabat (path "4" in Figures 2(A) and (B)) until the top of the convecting troposphere, above which the atmosphere is effectively isothermal (path "5" in Figures 2(A) and (B)). The liquid field is never encountered, and the optically thin atmosphere remains dry and at temperatures within ~80% of the surface of the magma ocean (Young et al. 2019).

Next we describe the factors controlling the rates of atmospheric escape and the optical depth of the lunar rock-vapor atmosphere. We evaluate the profile of the Na-rich rock-vapor atmosphere in P–T and P–S space using the rates of evaporation from the LMO and rates of atmospheric escape. We show that these rates conspire to keep pressures sufficiently low that the atmosphere behaves as in the "dry" path (paths "4" and "5") in Figure 2.

3.2.3. Mechanism of Atmospheric Escape from the Molten Moon

Because the density of the rock-vapor atmosphere above the LMO depends on the atmospheric escape rate, and the escape rate depends on the density, we start by way of an *ansatz* with

the structure of a thin atmosphere and then show that an optically thin atmosphere should have existed above the LMO. We consider first the case where we set the ground-level pressure above the magma ocean to 10^{-7} bar and the LMO surface temperature to 1800 K. We choose this initial example because our calculations suggest that these values maximize the likelihood for condensation while still being within the realistic pressure and temperature ranges for a steady-state atmosphere above the LMO, as shown below.

There are two main atmospheric escape mechanisms to balance evaporation at the surface of the LMO: hydrodynamic escape and Jeans' escape. Hydrodynamic escape involves a wholesale motion of collisional gas beyond the transonic point (r_s), where the gas sound speed (C_s) is about one-half the escape velocity (e.g., Hunten 1973; Zahnle & Kasting 1986; Hunten et al. 1987). The radius of the transonic point for an isothermal atmosphere is

$$r_s = \frac{GM_{Moon}}{2C_s^2} \tag{16}$$

where G is the gravitational constant and M_{Moon} is the mass of the Moon for our application.

The second mechanism of gas escape is Jeans' escape. Jeans' escape occurs at the exobase, defined as the region above which gas molecules are virtually collisionless and can escape to space given sufficiently high velocity. The altitude of the exobase can be specified for convenience as where the Knudson number (K_n), the ratio of the main free path of the gas molecules, l_{exo}, and the scale height, H_{exo}, is unity. The escape mechanism is determined by the relative heights of the
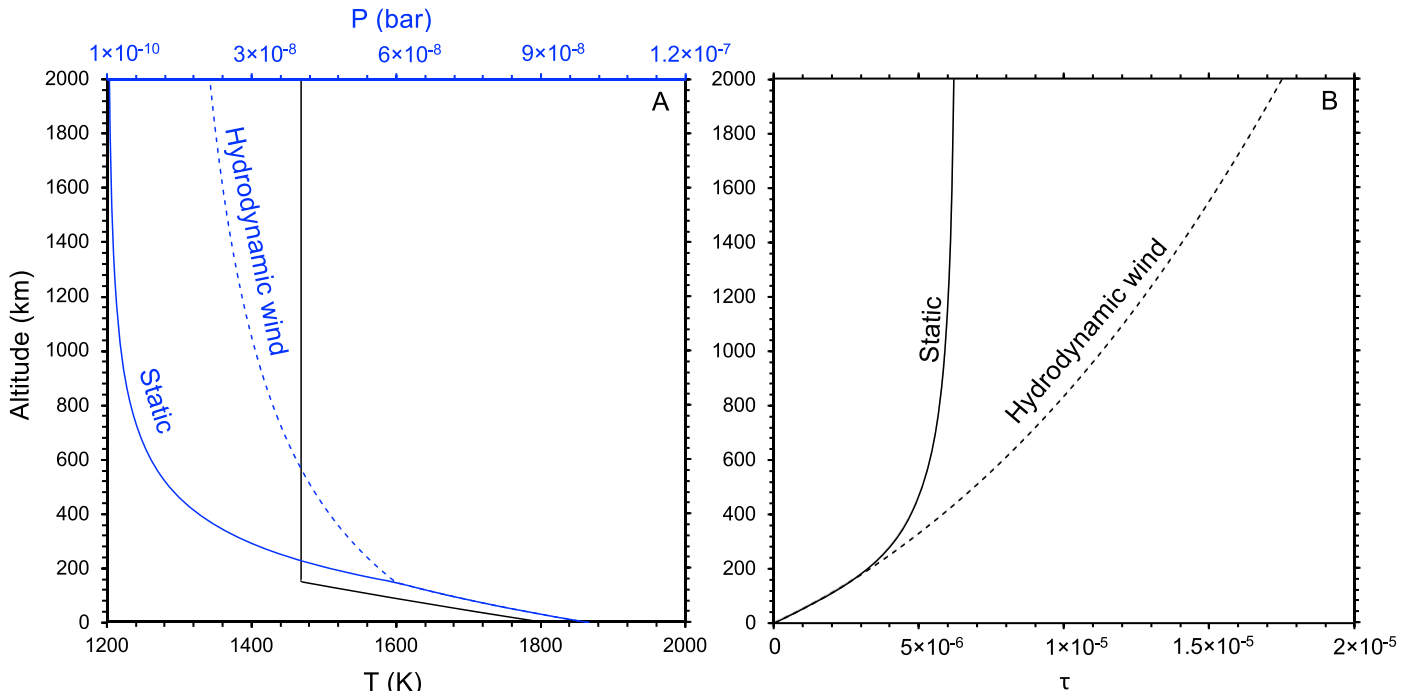
Figure 3. Temperature (T), pressure (P), and optical depth (τ) as functions of altitude above the LMO for a static atmosphere (solid lines) and the atmosphere including a hydrodynamic wind at the temperature of the isothermal heterosphere (dashed lines). The melt temperature is 1800 K, and the ambient pressure at ground level is 10^{-7} bar. With this T–P condition, the atmosphere is optically thin throughout, and the transonic point is at an altitude of 1800 km. Optical depth is based on the Rosseland mean opacity described in the text. In this example, the transonic radius is calculated based on Equation (16) for an isolated Moon without the effect from the Earth. The corresponding data file (ds04) can be accessed at doi:10.7910/DVN/LRIMT8.

transonic point and the exobase in the rock-vapor atmosphere. These relative positions depend on the mass of the body and the structure of the atmosphere. We note that both the transonic point and the exobase are in reality gradational and not precise radial positions.

In order to assess the relative positions of the critical radius for hydrodynamic escape and the exobase, we require at least a rough description of the rock-vapor atmosphere above the LMO. The altitude of the tropopause for our purposes is obtained using $P_{\text{tropopause}} \sim 0.6 P_{\text{o}}$ (Pierrehumbert 2010) where P_{o} is the surface pressure. Below the tropopause, convection prevails because of heating at the surface, and we can specify temperature variations with

$$\frac{dT}{dz} = -\frac{\gamma - 1}{\gamma} \frac{m_{\text{gas}} g}{k_B} \tag{17}$$

where z is the altitude above the surface and γ is the gas adiabatic constant ($\gamma = C_P/C_V = 5/3$ for ideal monatomic gas, and C_P and C_V are the isobaric and isochoric heat capacities). In the troposphere, we use the dry adiabat relating T and P:

$$\frac{d\ln(T)}{d\ln(P)} = \frac{R}{C_p}. \tag{18}$$

We justify using the dry adiabat in what follows by comparing the atmospheric escape rates to evaporation rates. Above the tropopause, radiation dominates heat transfer. Under an initial assumption of hydrostatic equilibrium (the validity of which is evaluated below with a numerical model), temperature and pressure vary with elevation z according to

De Pater & Lissauer (2006):

$$\frac{dT}{dz} = -\frac{3}{16} \frac{\alpha_{\text{R}} \rho_{\text{gas}}}{T^3} T_T^4 \tag{19}$$

where ρ_{gas} is the mass density of the gas, α_{R} is the Rosseland mean opacity, and T_{T} is the temperature at the tropopause ($z_{\text{T}} = 147$ km in this example). Since the mean opacity is only $\sim 0.001 \text{ m}^2 \text{ kg}^{-1}$ for Na gas at low densities of order $10^{-7} \text{ kg m}^{-3}$ (Freedman et al. 2008), the temperature variation in the stratosphere is expected to be minimal; in the first approximation, the atmosphere is nearly isothermal above the convective layer until reaching the escape layer. If the escape rate and attending upward flux of gas were to be relatively low, the pressure above the tropopause would be described by

$$\frac{d\ln(P)}{dz} = -\frac{1}{H} \tag{20}$$

where H is the scale height for a given altitude z given by $H = k_{\text{B}} T / (m \, g(r))$. We address departures from Equation (20) that lead to steeper pressure gradients that are due to a planetary "wind" associated with hydrodynamic escape in Section 4.1. The variations of temperature and pressure associated with altitude under these simplifying assumptions are shown in Figure 3(A). In this case, the temperature in the isothermal layer is determined to be ~ 1470 K, yielding values of 822 m s^{-1} and 1931 km for the sound speed (C_{s}) and the altitude of the transonic point r_{s}, respectively, for an average gas molecular mass of $0.030 \text{ kg mol}^{-1}$. The exobase lies well above the transonic point in this atmosphere (Figure 3(B)), suggesting that hydrodynamic escape, rather than Jeans' escape, will occur.

However, the relative efficacies of the two escape mechanisms are often evaluated using the escape parameter, $\lambda = (GMm_{gas}/r)/(k_b T(r))$, where M is the mass of the body and $T(r)$ is the temperature at radius r from the center of the body. The escape parameter is the ratio of gravitational energy to thermal energy. When evaluated at the surface of the body, λ_o, values $>\sim 4$–6 favor Jeans' escape over hydrodynamic escape (Volkov et al. 2011). In the case of the LMO, λ_o is ~ 5 for the Na-rich atmosphere considered here, with the precise value depending upon the temperature and exact mean molecular mass, suggesting that the thermal energy imparted to the gas by the magma ocean is marginally capable of overcoming the gravity well of the Moon for the relevant timescales. In what follows, we concentrate on hydrodynamic escape because of the probable influence of the Earth in exaggerating the efficacy of this process by lowering the altitude of the critical radius for escape, and because of the very high altitude of an exobase during active evaporation.

The optical depth (τ) integrated from the ground level upward is obtained from

$$\tau = \int_0^z \alpha_R \rho_{gas} \, dz, \tag{21}$$

and results are shown in Figure 3(B). At the transonic point, the optical depth is 6×10^{-6}, confirming the veracity of our *ansatz* that the atmosphere is optically thin where no condensation has taken place. The surface-integrated hydrodynamic flux (mol s^{-1}) through the escape layer is

$$J_{hydro} = 4\pi r_s^2 C_s \left(\frac{P_s}{RT} \right) \tag{22}$$

where subscript s signifies the quantity at the transonic point. In this case, the pressure at the transonic point is 2.4×10^{-9} bar and corresponds to an integrated hydrodynamic flux of 2.7×10^9 mol s^{-1}. The evaporative flux in this example calculated using our KNFCMAS code is 5.5×10^8 mol s^{-1}, or ~ 5 times lower than the surface-integrated escape rate. The presence of a hydrodynamic wind can fill up the upper atmosphere and enhance the hydrodynamic escape flux (Figure 3(A)). Our chosen example shows, therefore, that the steady-state pressure on the surface LMO must be lower than 10^{-7} bar. Higher surface pressures lead to an even higher ratio of escape flux to evaporative flux (Equations (4) and (21)), meaning that the steady-state atmospheric pressure is less than the 10^{-7} bar at the 1800 K used in this example.

The average molecular diffusion coefficient is of order 10^4 m^2 s^{-1} for the stratosphere pressures calculated here ($\sim 10^{-3}$ Pa, Figure 3). Typical values for k_{eddy} for a large spectrum of planetary environments are on the order of 1 to 100 m^2 s^{-1} at pressures $<10^{-5}$ bar (1 Pa; Zhang & Showman 2018), and they are orders of magnitude smaller than the molecular diffusivity above the tropopause here. This suggests that the lunar rock-vapor stratosphere was a poorly mixed heterosphere. Expressed in terms of pressure, Catling (2015) points out that the homopause for planetary bodies generally occurs at pressures within an order of magnitude or two of 10^{-7} bar (10^{-2} Pa), and Yamanaka (1995) suggests similar homopause pressures of about 10^{-6} bar (0.1 Pa) for a range of planetary atmospheres. Nakajima & Stevenson (2018) arrive at a broadly similar range of homopause pressures of 10^{-9}–10^{-4} bar (10^{-4}–10 Pa). The rock-vapor atmosphere above the tropopause as calculated here was therefore likely to be a heterosphere. For the atmosphere above the LMO, the tropopause

was effectively the homopause, the troposphere was the homosphere, and the stratosphere was the heterosphere.

Raising the temperature in our example to 2000 K brings the evaporative flux close to the escape flux, approaching steady state. In order to solve for the steady-state density of the rock-vapor atmosphere above the LMO over the range of temperatures considered in this study, and in so doing evaluate the likelihood for alkali-rich rain, we must first examine the influence that the Earth had on the rate of atmospheric escape from the molten Moon.

3.2.4. Earth's Influence on Hydrodynamic Escape

In order to explore further the conclusion that hydrodynamic escape from an optically thin rock-vapor atmosphere is the most likely mechanism that balanced the evaporative flux from the LMO, we require a more detailed analysis of hydrodynamic escape rates and the influence that the proximal Earth would have had on these rates. The Moon did not form in isolation, and the presence of the Earth played a role in facilitating hydrodynamic escape, and thus potentially loss of MVEs from the Moon. Previous models suggest that the Earth–Moon distance was only $\sim 5\%$–10% of the present distance ($\sim 20{,}000$–40,000 km, e.g., Canup et al. 2015; Lock et al. 2018) immediately following the Moon-forming impact. The radial position of the Moon's Hill sphere relative to the Earth is

$$R_H = a_{Earth-Moon} \left(\frac{M_{Moon}}{3M_\oplus} \right)^{\frac{1}{3}} \tag{23}$$

where $a_{Earth-Moon}$ is the Earth–Moon distance at the time that melt was still exposed at the surface of the Moon. At the Moon's Hill sphere, the Moon's gravitational force and Earth's perturbing tidal force are approximately equivalent. In detail, for gas molecules between Earth and Moon, the gravity of the Earth is partly opposed by a centrifugal force. The gravitational influences of the Earth's gravitational force and the centrifugal forces act to lower the position of the transonic point in the LMO atmosphere and increase the rate of hydrodynamic escape. We solve for the relationship between the critical transonic radius for the molten Moon's rock-vapor atmosphere (r_c) and the Earth–Moon distance ($a_{Earth-Moon}$) when the Moon was proximal to the Earth.

The equations of mass and momentum conservation in a steady-state atmosphere are

$$\frac{dM_{gas}}{dt} = 4\pi r^2 \rho \cdot v \tag{24}$$

and

$$\rho v \frac{dv}{dr} = -\rho \frac{d\phi}{dr} - \frac{dP}{dr}, \tag{25}$$

where M_{gas} is the total mass of the atmosphere vapor, v is gas velocity, ρ is gas density, r is the radial distance from the Moon's center, P is pressure, and ϕ is effective gravitational potential. For gas loss on an isolated planetary body, the gas velocity approaches the sound speed, and we can write

$$\left(\frac{d\phi}{dr} \right)_{r=r_s} = \frac{2C_s^2}{r_s}. \tag{26}$$

The detailed derivation of Equation (26) can be found in Appendix C. Equation (26) can be rewritten as Equation (16) to solve for r_s where no exogenous gravitational forces are present. For the Earth–Moon system, we consider the effective gravitational potential at a point r located between the Earth and Moon, taking account of the gravity from the Earth and the Moon as well as the centrifugal forces attributed to the rotation around the Earth. The gravitational acceleration at the point r is then

$$\frac{d\phi}{dr} = \frac{GM_{\mathrm{Moon}}}{r^2} - \frac{GM_\oplus}{(a_{\mathrm{Earth-Moon}} + r)^2} + \frac{GM_\oplus}{a_{\mathrm{Earth-Moon}}^3}(a_{\mathrm{Earth-Moon}} - r). \tag{27}$$

By equating the accelerations in Equations (26) and (27), one can solve for r where it equals the transonic point, or critical radius r_c, so that the influence of the Earth is now included in the position of the transonic point (Appendix C and Figure 4). In our case, when T_{LMO} ranges from 1800 to 2000 K, the ratio of the transonic radius calculated from Equations (26) and (27) compared to the radius calculated based on Equation (16) alone for an isolated Moon, r_c/r_s, varies with Earth–Moon distance. Figure 4 shows the variation for Earth–Moon distances of 5%–18% of the present value (~20,000–70,000 km, or 3.1–11.0 $R_\oplus$). Where the Earth–Moon distance is large and the effect from Earth is negligible, $r_c = r_s$ (Figure 4). However, where the Moon is at a minimum distance corresponding to just beyond the Roche limit ($a_{\mathrm{Earth-Moon}} = 20,000$ km), vapor escape from the Moon is significantly affected by the gravity of the Earth, as indicated by $r_c \sim 0.62 \, r_s$ (Figure 4). Other cases lie between these two asymptotes. Altitudes of the transonic point, z_c, over the range of surface magma ocean temperatures (1800–2000 K) considered here and for Earth–Moon distances ranging from just beyond the Roche limit at 5% of the present distance to 18% of the present distance where Earth's influence becomes negligible are shown in Figure 5. The altitude of the transonic radius is calculated to have been from 447 to 1800 km above the surface of the LMO. At the minimum Earth–Moon distance just beyond the Roche limit and with high melt temperatures (e.g., 2000 K), the altitude for the transonic point would have approximately coincided with the Moon's Hill sphere. Only when the Earth–Moon distance is several times greater than the Roche limit is the effect from the Earth negligible.

The position of the transonic point can be used to calculate the hydrodynamic escape flux from the Moon as before but evaluated at r_c:

$$J_{\mathrm{esc}} = 4\pi (r_c)^2 C_s \left(\frac{P_c}{RT_T}\right), \tag{28}$$

where P_c is the pressure at the transonic radius r_c, and T_T is the temperature of the tropopause that extends upward through the radiative, isothermal layer. Note that Equation (28) is applicable for $P_c > \sim 10^{-11}$ bar. If $P_c \leqslant \sim 10^{-11}$ bar, Jeans' escape must be taken into account as the competing mechanism of gas escape.
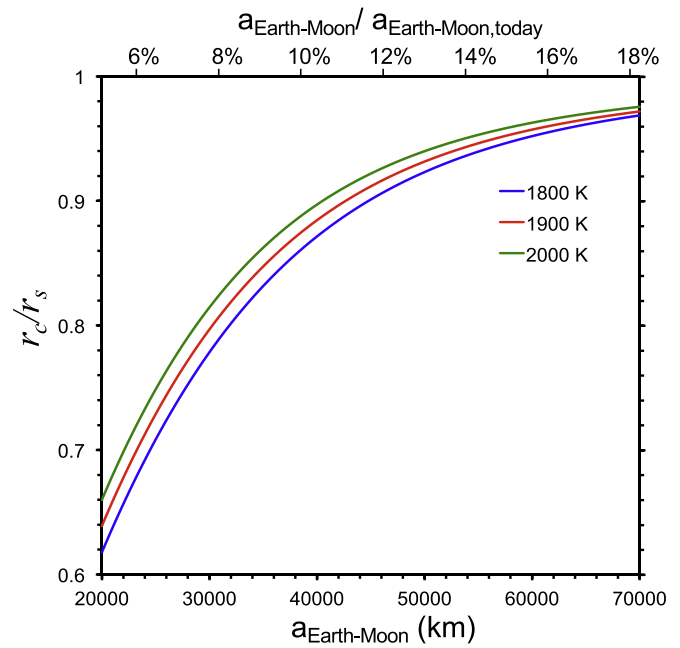

Figure 4. Ratio of the critical point (r_c) determined by Equations (26) and (27) for the lunar rock-vapor atmosphere and the transonic radius (r_s) for an isolated Moon as functions of Earth–Moon distance and T_{LMO} ranging from 1800 to 2000 K. The increase in the ratio r_c/r_s toward unity with Earth–Moon distance indicates that recession of the early Moon diminished the Earth's effect on the transonic radius for the atmosphere above the LMO. The corresponding data set (ds05) can be accessed at doi:10.7910/DVN/LRIMT8.

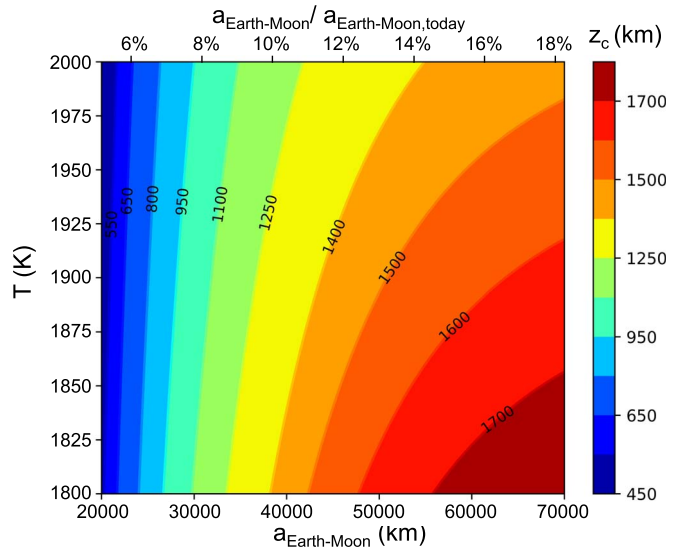**Figure 5.** Altitude of the critical radius for hydrodynamic escape above the LMO corresponding to different Earth–Moon distances (5%–18% of $a_{\mathrm{Earth-Moon,today}}$) and surface melt temperatures (1800–2000 K) as calculated from Equations (26) and (27). A short Earth–Moon distance lowers the altitude of the critical radius. The data for this contour plot (ds06) can be accessed at doi:10.7910/DVN/LRIMT8.

3.2.5. The Steady-state Atmosphere

The rate of evaporation from the surface magma ocean and the rate of atmospheric escape have negative and positive correlations with pressure, resulting in a steady-state rock-vapor atmosphere. Figure 6 shows the variation of surface-integrated net evaporative flux and integrated gas loss flux for
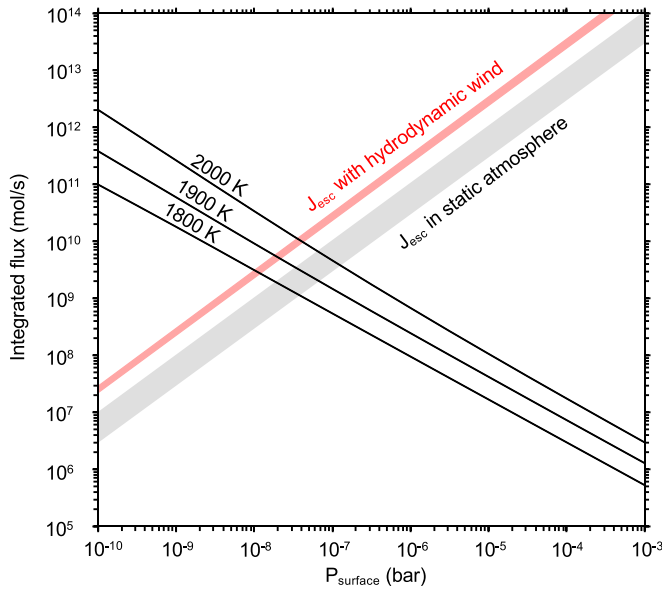
Figure 6. Determination of steady-state near-surface pressures of the lunar rock-vapor atmosphere based on the equivalence of the surface-integrated net evaporative fluxes of Na-rich vapor (black lines) with surface-integrated hydrodynamic escape fluxes. The latter escape fluxes are based on pressures using a static atmosphere approximation (gray bar) and pressures including the hydrodynamic wind (red bar) at the transonic point. Three temperatures spanning the relevant range of 2000–1800 K are shown for illustration. The steady states are given by the crossovers where the fluxes are equal and correspond to pressures of 10^{-8} to $\sim 10^{-7}$ bar. The corresponding data set (ds07) can be accessed at doi:10.7910/DVN/LRIMT8.

hydrodynamic escape beyond the transonic radius r_c for surface temperatures of 2000, 1900, and 1800 K and Earth–Moon distances ranging from 5% to 18% of $a_{\text{Earth–Moon, today}}$ (20,000–70,000 km). The crossing points of these curves define steady-state ambient pressures (the pressure directly above LMO in this context). Figure 6 shows that the surface pressures directly above the LMO would have ranged from 10^{-7} to $\sim 10^{-8}$ bar at steady state. Due to the hydrodynamic escape flux beyond the critical point, these ground steady-state pressures are considerably less dense than that calculated using thermodynamic equilibrium pressures by Saxena et al. (2017; $\sim 10^{-3}$–10^{-1} bar). These steady-state pressures validate our previous assertion that the atmosphere above the LMO was alkali rich, dry, and optically thin.

The steady-state atmospheric surface pressures and temperatures allow us to trace the atmosphere in P–T and P–S space with altitude from the ground level to the escape layer (Figures 7(A) and (B)). Over the range of temperatures considered here for the magma ocean surface, the rock-vapor atmosphere remains undersaturated with respect to liquid, and no Na oxide rain is expected to have occurred throughout the atmosphere column up to the point of escape. The same is true for oxides of K (Figures 7(A) and (B)).

Purely adiabatic expansion where the sole source of energy is the internal energy of the gas itself is unlikely. If the rising atmosphere were to have expanded adiabatically, then the relation $P^{1-\gamma}T^{\gamma} = $ constant, where $\gamma = C_P/C_V = 1.66$ for our Na-dominated atmosphere, indicates that the atmosphere would cool to ~ 800 K and therefore reach saturation at altitudes beyond about 1000 km above the surface. Alkali rain would therefore stymie escape when the critical radius is beyond this point. However, the magma ocean surface radiates at 10^{19} W

for the period that a large fraction of the surface remains above the solidus. For a mean opacity of 0.001 m² kg^{-1}, a median gas density of 10^{-7} kg m^{-3} for the relevant pressures, and a path length through the atmosphere of 1000 km from the homopause to the critical radius, excluding the effects of Earth in this example, the atmosphere, despite being optically thin, will have absorbed 0.01% of this power, or 1×10^{15} W (this value scales with the fraction of exposed melt). The power loss by atmospheric escape in the form of gravitational potential energy and thermal energy, $\dot{E}$, is

$$\dot{E} = \frac{GM}{r_c}\dot{m} + \frac{k_b T}{n}\dot{n}. \tag{29}$$

For the surface-integrated loss rate of $\dot{n} = 2 \times 10^{33}$ molecules s^{-1} (e.g., Figure 6), there should have been 8×10^{13} W leaving the system, showing that the energy gained from the magma ocean, $\sim 10^{15}$ W, easily offsets the energy loss due to expansion; cooling of the escaping gas is not the primary source of energy for expansion above a magma ocean.

While evaporation persists, so does the steady-state atmosphere. At the steady-state surface pressures of 10^{-8}–10^{-7} bar, K isotope fractionation factors based on Equation (7) have approximately equilibrium values (Figure 1(B)). Near-equilibrium evaporation generates a K isotopic composition in the LMO indistinguishable from the initial, presumably terrestrial, ^{41}K/^{39}K value. An alternative to simple evaporation is required to explain the high ^{41}K/^{39}K of lunar samples if they derive from the existence of the LMO exposed to space.

4. Isotope Fractionation in the Atmosphere

4.1. Hydrodynamic Escape

Having shown that evaporation from the LMO is not a viable mechanism to cause the observed heavy isotope enrichment in the Moon, we turn to the alternative of fractionation of the overlying rock-vapor atmosphere. The near-equal fluxes of MVE molecules from melt to vapor and from vapor to melt that arise as a result of evaporation into a steady-state rock-vapor atmosphere allow for isotopic exchange between melt and vapor. Indeed, it is this exchange that leads to the near-equilibrium vapor–melt isotope fractionation factor. Therefore, if isotope fractionation was present in the atmosphere, this fractionation could have been imparted to the partially molten surface of the Moon by melt–vapor exchange.

Hydrodynamic escape involves a wholesale motion of the gas molecules whereby isotopic fractionation relies on the ratio of the mutual diffusivity to total flux (Hunten 1973; Zahnle & Kasting 1986; Hunten et al. 1987). The interactions among the molecules yield essentially a single sound speed for all constituent species. In a Na-rich vapor such as that considered here, the fractionation factor between potassium atoms and the average molecular mass can be estimated using

$$\alpha_{\text{hydro}} \sim 1 - \frac{GM_{\text{Moon}}(m_K - m_{\text{avg}})D_K n_{\text{gas}}}{C_s n_{\text{gas}} r_c^2 k_B T} \tag{30}$$

where n_{gas} refers to the number density of the gas at the transonic point, and the high-flux approximation of Zahnle & Kasting (1986) is employed here. With $m_{\text{avg}} = \sim 0.030$ kg mol^{-1} for the Na-abundant rock-vapor atmosphere (3–6 mol% of K), Equation (30) yields a ^{41}K/^{39}K isotopic fractionation factor very near 1.000,
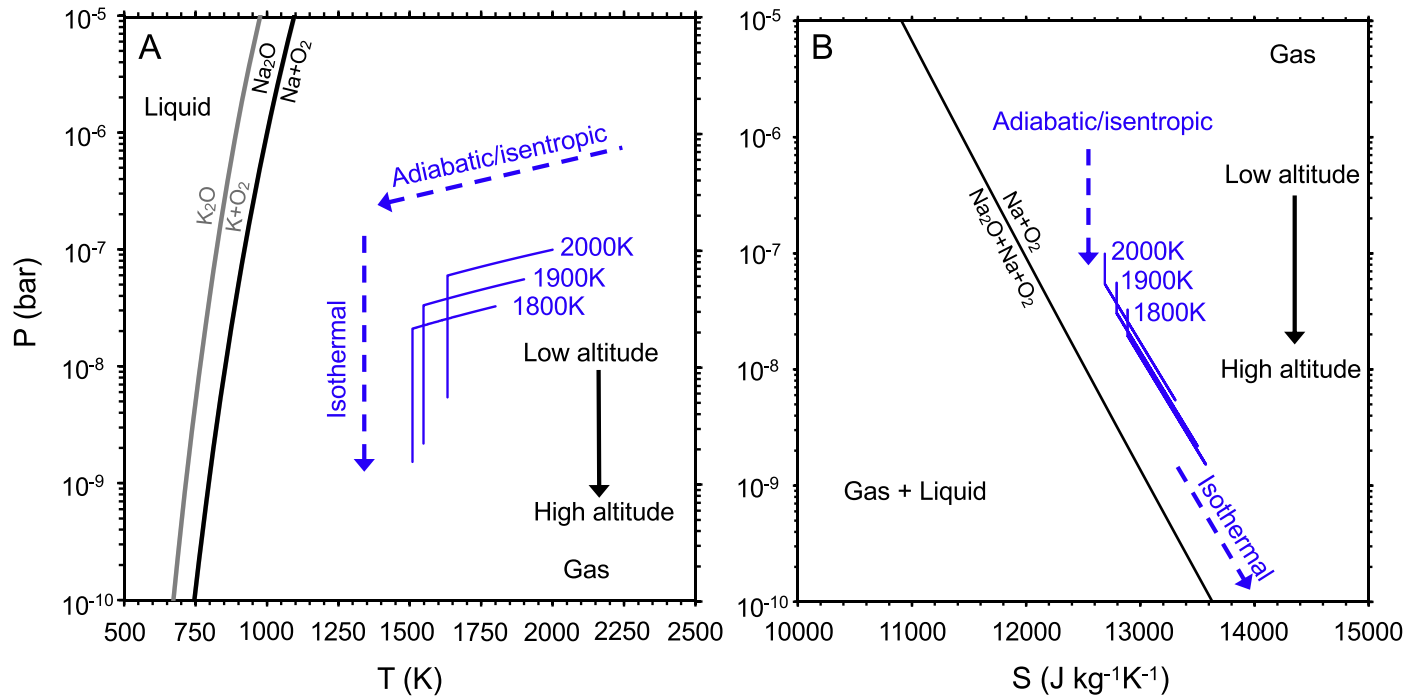
Figure 7. Quantitative P–T (A) and P–S (B) phase diagrams showing variations with increasing altitude for the steady-state lunar Na-dominated rock-vapor atmosphere. Melt temperatures range from 1800 to 2000 K. The blue lines indicate the variations of P, T, and S for the atmosphere from the surface LMO to the isothermal stratosphere. The terminations of each of the pathways at low pressures represent the maximum altitudes where the transonic point z_c is encountered for $a_{\mathrm{Earth-Moon}} = 70{,}000$ km. The Earth–Moon distance is not an important factor in determining the steady-state pressure compared to the influence of melt temperature; changing the Earth–Moon distance does not alter the basic relationships shown in this example. These calculations are for the pure Na–O system. The liquid–vapor phase boundary for the K–O system is shown for comparison. The corresponding data set (ds08) can be accessed at doi:10.7910/DVN/LRIMT8.

implying that the process of hydrodynamic escape of alkali vapor cannot alone result in a resolvable K isotopic fractionation.

Despite the implications of Equation (30), the presence of a sizable heterosphere below the critical radius for escape warrants examination. It is conceivable that some fractionation could occur due to gravitational settling even in the face of the outward hydrodynamic wind, or "Parker wind," attending the escape. The velocity increases upward from the surface under these circumstances, and at lower altitudes g can compete more effectively with the slower upward velocity. In order to investigate the competition between the planetary wind and settling, we solve for the 1D isothermal, steady-state planetary wind velocities, u, with radial distance from the center of the body using (Parker 1964)

$$\frac{u^2}{C_s^2} - \ln\left(\frac{u^2}{C_s^2}\right) = -3 + 4\ln\left(\frac{r}{r_c}\right) + 4\frac{r_c}{r} \qquad (31)$$

together with $\partial n_i / \partial t = -\nabla J_i$, where ∇J_i is the divergence of the hydrodynamic and diffusive fluxes at each radial position. The full expression for the number density of species i at each radial position in the heterosphere is

$$\begin{aligned}
\frac{\partial n_i}{\partial t} &= -\frac{\partial}{\partial r}(u n_i) - \frac{\partial}{\partial r}\left(-(D + k_{\mathrm{eddy}})\frac{\partial n_i}{\partial r}\right) + \frac{\partial}{\partial r}(w_i n_i) \\
&= -u\frac{\partial n_i}{\partial r} - n_i \frac{\partial u}{\partial r} + (D + k_{\mathrm{eddy}})\left(\frac{\partial^2 n_i}{\partial r^2} + \frac{2}{r}\frac{\partial n_i}{\partial r}\right) \\
&\quad + \frac{\partial n_i}{\partial r}\frac{\partial}{\partial r}(D + k_{\mathrm{eddy}}) + w_i \frac{\partial n_i}{\partial r} + n_i \frac{\partial w_i}{\partial r}.
\end{aligned}$$
$$(32)$$

Here, D is the molecular diffusion coefficient evaluated as b_i / n_{gas}, where b_i is the mass-dependent binary diffusion parameter (Pierrehumbert 2010), n_{gas} is the total number density, and w_i is the terminal velocity of the gas molecules evaluated as $w_i = gl/\sqrt{kT/m_i}$ where $g = GM_{\mathrm{Moon}}/r^2$ and l is the mean free path at radial position r. Where u is zero, Equation (32) yields purely hydrodynamic equilibrium where the diffusion-limited pressure gradient balances gravitational settling. Where u is greater than zero, the upward flow due to the pressure gradient mitigates the effects of diffusion and gravitational settling. The extent of this mitigation increases upward as the gas accelerates (Equation (31)) and g decreases. We include turbulent diffusion, k_{eddy}, because despite the convenience of simply defining the homopause as where $k_{\mathrm{eddy}} \sim D$, various studies demonstrate that k_{eddy} can be significant even above the homopause (in effect, the turbopause and homopause are not identical). For example, Slipski et al. (2018) used MAVEN data to show that in the Martian heterosphere, k_{eddy} values of order 10–10^4 m^2 s^{-1} occur in the vicinity of the homopause. Here we present results with a fixed k_{eddy} of 10^2 m^2 s^{-1}, but this value has only a small influence on the results shown here. Values of 10^5 are required to significantly alter these results, and the effect is to further reduce fractionation by mass.

We solved Equations (31) and (32) using implicit finite difference. The lower boundary condition is the constant pressure at the homopause (equals the tropopause) prescribed by our evaporation calculations (taken to be 1×10^{-8} bar). If evaporation were to cease, there would no longer be a steady-state atmosphere. A constant-flux upper boundary condition
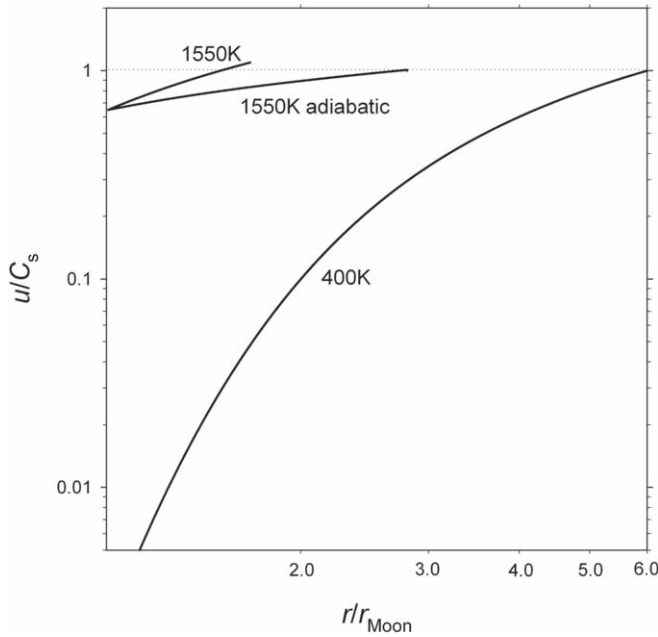
Figure 8. Velocity profiles in terms of u/C_s vs. r/r_{Moon} for isothermal heterospheres with temperatures of 1550 and 400 K and an adiabatic atmosphere with a homopause temperature of 1550 K. The corresponding data set (ds09) is provided at doi:10.7910/DVN/LRIMT8.

was used. Different but similar upper boundary conditions, including a constant low pressure, give the same results: gas passes through the system as required by the velocity profile obtained from Equation (31). The initial condition was a low pressure of 10^{-16} bar, but an initial condition of a static atmosphere at hydrodynamic equilibrium yields identical results once a steady-state profile is achieved. The Python code for atmospheric escape calculations (Atmosphere_Cs_v9) is provided at doi:10.7910/DVN/LRIMT8.

We obtained the number densities of ^{23}Na, ^{41}K, and ^{39}K simultaneously as functions of t and r. Model timescales correspond to years; all of the results presented here are for a steady state. Results are presented for two homopause temperatures, 1550 and 400 K. In one case the heterosphere is isothermal with a temperature of 1550 K, as suggested by our atmosphere structure described above. For comparison, an isothermal heterosphere at 400 K is shown to represent the other extreme of a low-temperature atmosphere above the homopause. Temperatures much lower than 400 K do not lead to escape in the time frames of interest here. In addition, we present results for adiabatic expansion from 1550 K at the homopause to ∼400–600 K at the transonic point. The latter is an approximation obtained by solving Equation (31) iteratively at each radial position and associated temperature to achieve a self-consistent velocity and temperature profile.

We show results for Earth–Moon distances of 10% and 100%. Figure 8 shows the velocity profiles for the three temperature profiles in terms of u/C_s versus r/r_{Moon} for comparison with velocity profiles from previous studies (e.g., Zahnle & Kasting 1986; Tian & Toon 2005). The low-T isothermal case represents a high λ_o value of 20. Such a high value would disfavor hydrodynamic escape for this Na-rich atmosphere, but escape is possible if evaporation continues for sufficient time to establish the steady-state atmosphere.
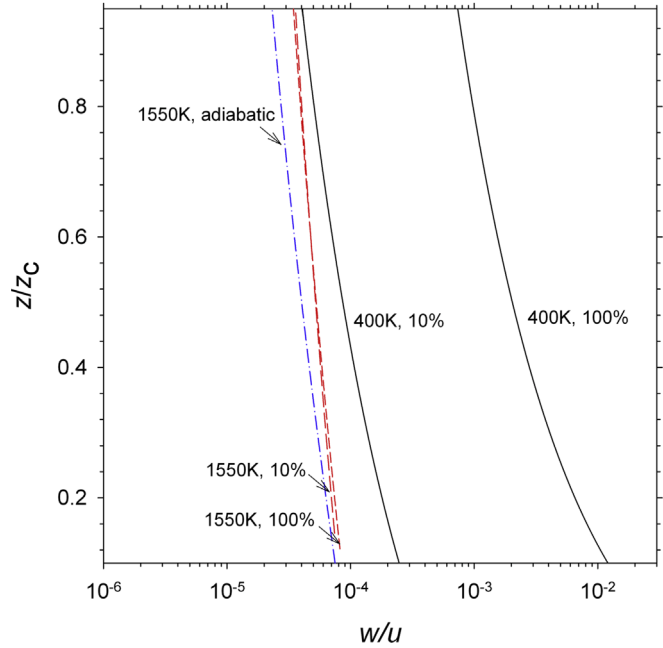

Figure 9. Ratio between terminal velocity (w) and the total upward velocity (u) as functions of atmospheric altitude (z) relative to the critical point (z_c) for isothermal heterospheres with temperatures of 1550 K (red dashed lines) and 400 K (black solid lines). For each temperature we simulate w/u with 10% and 100% of the present Earth–Moon distance. We also show the w/u profile for a polythermal heterosphere with $T_{homo} = 1550$ K and adiabatic expansion. All profiles start from P_{homo} of 10^{-8} bar. Among all five profiles, only the 400 K isothermal case with the present Earth–Moon distance yields terminal velocities capable of competing against the upward hydrodynamic wind. The corresponding data set (ds09) is provided at doi:10.7910/DVN/LRIMT8.

In a static atmosphere, hydrodynamic equilibrium for gaseous species i above the homopause is defined by

$$n_i = n_i^o \exp\left(\frac{r}{H_i} - \frac{r^o}{H_i^o}\right) \qquad (33)$$

where superscript o signifies evaluation at the homopause, and scale height H_i is given by $H_i = k_B T/(m_i\, g(r))$. The addition of an upward flux u steepens the gradient, as shown in Figure 3.

The time required to achieve hydrostatic equilibrium in a static atmosphere depends on the rate of diffusion. The characteristic timescale (τ) for diffusive equilibration can be obtained from $h = \pi\sqrt{D_K \tau}$ (e.g., Giunta et al. 2017), where h is the scale of the isothermal heterosphere and D_K is the average diffusivity of K in the isothermal layer. For an LMO temperature of 1800 K and $a_{Earth-Moon}$ of 70,000 km, an average diffusivity of K of 4.6×10^4 m^2 s^{-1}, and a heterosphere depth of ∼1600 km, the timescale τ for gravitational settling of K is ∼65 days. This comports with the short timescales obtained in our numerical model; steady-state profiles of fractionated gas will have occurred above the LMO on timescales of days to a year.

The prospects for fractionation by molecular mass depend on the relative magnitudes of the total upward velocity u and the terminal velocities w_i. Figure 9 shows the ratio w_i/u for Na versus height above the surface starting at the homopause. In the low-T isothermal case, w_i/u is sufficiently large that some mass fractionation is possible. However, this low temperature that permits fractionation cannot arise from simple adiabatic expansion; both an isothermal 1550 K heterosphere and a 1550 K homopause with adiabatic expansion render gravitational settling ineffectual
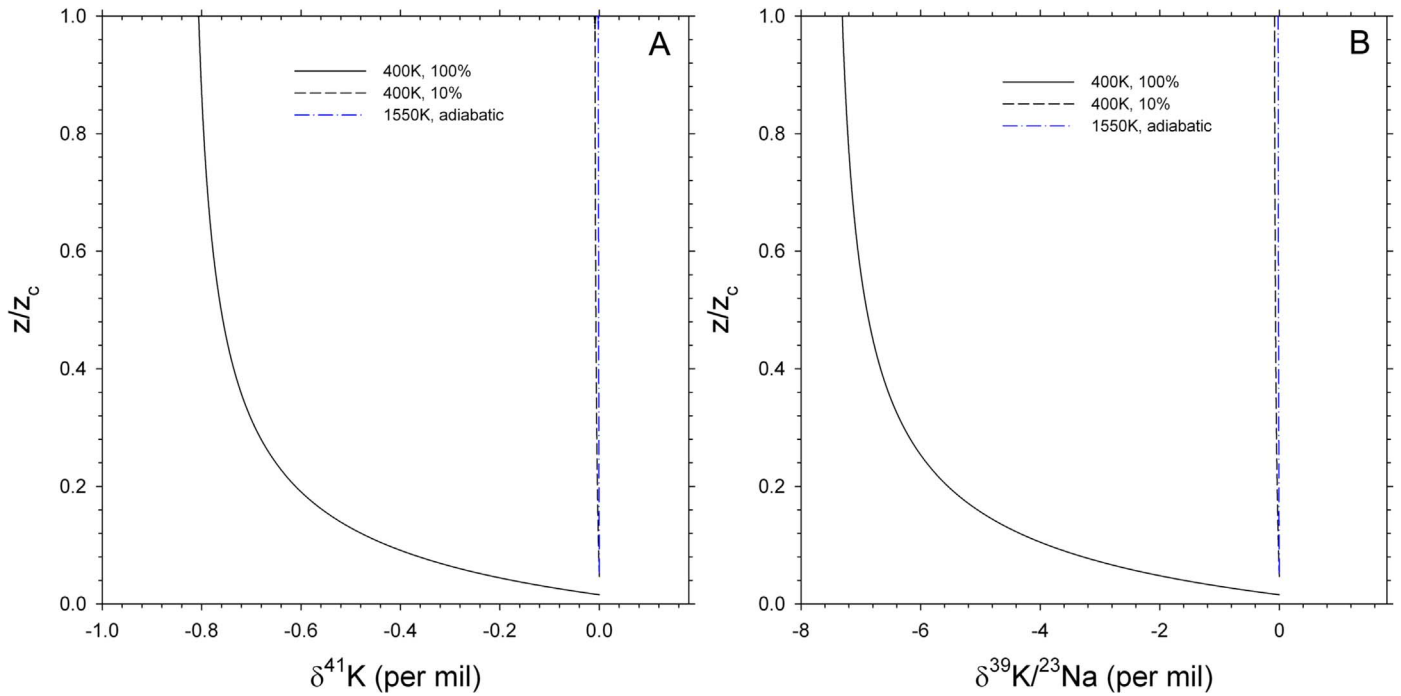
Figure 10. Altitude profiles for the relative abundances of K compared to Na (A) and K isotope ratios expressed as δ^{41}K (B). Altitude (z) is shown relative to the critical point (z_c). For an adiabatically expanding heterosphere with $T_{\mathrm{homo}} = 1550$ K (blue dashed lines) and an isothermal heterosphere with short Earth–Moon distance (10% of the present distance as the example here, black dashed lines), strong hydrodynamic winds will homogenize the entire atmosphere. Only a low temperature with negligible gravitational effects from the Earth can generate detectable chemical and isotopic fractionations due to gravitational settling (black solid curves). The corresponding data set (ds09) is provided at doi:10.7910/DVN/LRIMT8.

(Figure 9). This is because the fractionation at low temperature is most efficacious at low altitudes.

The fractionations of K from Na and ^{41}K from ^{39}K in the heterosphere are shown in Figures 10(A) and (B), respectively. Only in the cool, isothermal heterosphere is the mass separation sufficient to yield a measurable effect on the escaping atmosphere. At 400 K, the largest shift in δ^{41}K associated with the escaping gas is about -0.8 per mil when the Earth–Moon distance is 100% of today. The associated shift in K/Na is nearly -7.5 per mil. Under the more realistic scenario of a hotter homopause, 1550 K in our calculations, the absolute values for both shifts in ratios are $\ll 0.1$‰.

Isotope fractionation in the heterosphere is aided by a greater Earth–Moon distance. However, we point out that while fractionation at low temperature is feasible based on these escape calculations alone, we have shown that at the pressures that likely existed in the heterosphere, such a low temperature would lead to condensation of alkali vapor high in the atmosphere, greatly reducing the prospects for isotopic and elemental fractionation among the alkali elements.

We performed mass-balance calculations showing that with an atmospheric δ^{41}K value of ~ -1‰, the maximum feasible absolute value, and requiring low temperatures at the homopause, the steady-state evaporation and atmospheric loss would need to have been active for at least 10^4 yr (assuming [K]$_{\mathrm{Moon}} = 50 \,\mu$g g^{-1} and K/Na = 0.1 in the vapor). This is longer than the interval where the LMO should have been exposed to space. Thus, we find that hydrodynamic escape above evaporated LMO cannot have fractionated lunar MVE isotopes.

4.2. Wet versus Dry Moon

In this work we assume an essentially dry Moon as the initial condition. Although we did not include water in the

calculations above, we evaluated the likelihood for an initially dry, rather than wet, LMO by estimating the timescale required to vaporize water from the vigorously convecting melt. We calculated the escape flux of a water-rich vapor for the early Moon near the Roche limit, assuming the earliest Moon formed there, and estimated the timescale to vaporize all of the water from the bulk LMO. The evaporative flux of H_2O in the melt can be estimated using the Hertz–Knudsen equation and the relative equilibrium vapor pressures of Na and H_2O. Water has a considerably higher equilibrium vapor pressure above the melt compared with the alkalis at relevant temperatures, with $P_{H_2O} > 10^3 P_{Na}$ at 2000 K (Herbort et al. 2020). At the Roche limit with $T \sim 2000$ K, the atmosphere evaporated from a water-rich LMO ([H_2O] $\sim 700 \,\mu$g g^{-1}, consistent with the minimum estimate for the BSE; McCubbin & Barnes 2019) would mainly consist of water vapor with an average molecular mass of ~ 0.018 kg mol^{-1}. For $T_{\mathrm{LMO}} = 2000$ K and $a_{\mathrm{Earth-Moon}}$ just beyond the Roche limit (~ 5% of the present distance), the steady-state background pressure and corresponding escape flux of the water-rich gas are estimated to be $\sim 1.5 \times 10^{-6}$ bar and $\sim 4 \times 10^{11}$ mol s^{-1}, respectively. The altitude of the critical radius is ~ 60 km above the LMO. Based on these calculations, the early Moon may have had a narrow, well-mixed water-rich atmosphere, although for only a brief time. The high escape rate will have resulted in a rapid loss of water. It should have taken just ~ 150 yr to reduce the water concentration in the whole of the LMO melt from 700 μg g^{-1} to 100 μg g^{-1} with this nonequilibrium, steady-state atmosphere. This timescale is one to two orders of magnitude shorter than that required to lose 80% of K and Na from the melt with Earth-like initial concentrations. For the LMO depleted in H_2O (e.g., [H_2O] $\sim 100 \,\mu$g g^{-1}), losing 90% of the water in the melt requires just ~ 60 yr. Thus, one can expect that the proto-

Moon may have lost water and become dry prior to forming an Na-rich rock-vapor atmosphere. Nonetheless, future work is required to investigate the isotopic effects of an atmosphere composed of volatiles (e.g., H_2O, CO_2, CO) and rock vapor.

5. Implications for the Origin of the Moon

Isotope fractionation by evaporation and vapor escape above the LMO is but one of several candidate processes for influencing the chemical and isotopic composition of the Moon. It operated during a short interval after condensation of the Moon once the LMO was exposed to space. We find that this process was ineffective, and in future alternative processes it should be considered to explain the concentration depletions and heavy isotope enrichments of the lunar MVEs. The proto-Moon may have accreted rapidly inside a vapor–melt structure generated through the giant impact beyond the Roche limit with a temperature of 3000–4000 K and high ambient pressures of up to ~100 bar (e.g., Lock & Stewart 2017; Lock et al. 2018). Under these conditions, incomplete condensation may have determined the overall concentrations of the MVEs in the Moon but with no resolvable isotope effect (saturation at high temperatures), or a preference for light isotopes due to the greater collision frequency of the latter with condensing surfaces (supersaturation; Taylor et al. 2006; Pahlevan et al. 2011). In this scenario, subsequent contraction of the structure exposed the nascent Moon to space. The sharply decreased ambient pressure would have initiated evaporation of the magma ocean, resulting in rapid build-up of an atmosphere dominated by volatile, and then moderately volatile, elements. Our analysis combined with the well-known isotopic consequences of condensation suggests that none of these processes could have caused the observed heavy isotope enrichments in lunar MVEs.

The potential effect on the chemical and isotopic fractionation occurring in a protolunar melt disk prior to the accretion of the Moon is another important process to consider (e.g., Canup et al. 2015). A recent model suggests that the gas viscosity associated with MRI could explain the isotopic fractionation of MVEs in the Moon assuming a partially vaporized protolunar disk (Nie & Dauphas 2019). In any event, evaporation from the LMO exposed to space is not a viable mechanism for fractionation of K and other MVE isotopes.

Although the near-equilibrium elemental and isotope fractionation factors obtained in this analysis were inconsequential for the Moon because of the transient nature of the LMO, they may prove to be important where denser atmospheres prolong the magma ocean phase on other bodies. This study provides a basis for the simplifying assumption that even with vigorous atmospheric escape, a boundary layer of gas in equilibrium with melt is likely where a magma ocean is extant.

6. Conclusions

In this work, we explore the efficacy of escape from a tenuous rock-vapor atmosphere as a mechanism for affording isotope fractionation of MVEs from the Moon. We find that vapor pressure should have built up adjacent to the surface of the LMO once it was exposed to space. The resulting atmosphere would have inevitably led to near-equilibrium isotope partitioning between the evaporated vapor and the silicate melt at pressures of 10^{-7}–10^{-8} bar with T_{LMO} of 2000 K to 1800 K. Hydrodynamic escape from this quasi-steady-state, optically thin atmosphere would not cause a

measurable fractionation except possibly under unrealistically low temperatures and approximately isothermal conditions.

Appendix A
Derivation of Equation (7) for Net Evaporation Isotope Fractionation Factor

The evaporative flux of a species i from a melt is given by the Hertz–Knudsen equation:

$$J_{i,\text{net}} = \frac{\gamma_i(P_{i,\text{eq}} - P_i)}{\sqrt{2\pi m_i RT}} \qquad (A1)$$

where $P_{i,\text{eq}}$ is the equilibrium vapor pressure of gas species i, P_i is the actual vapor pressure, m_i is the molecular mass of species i, γ_i is the evaporation coefficient for i, R is the ideal gas constant, T is temperature, and $J_{i,\text{net}}$ is the net evaporative flux of gas species i. The γ_i parameter that appears in the evaporation equations is akin to the sticking coefficient for adsorption. Equation (A1) shows that the net flux of a species i from the surface of an evaporating body, $J_{i,\text{net}}$, is the difference between the free evaporative flux, $J_{i,\text{evap}}$, which is proportional to the equilibrium vapor pressure, and the return flux $J_{i,\text{return}}$, which is proportional to the local partial pressure P_i. The return flux leads to a pressure build-up adjacent to the surface of the evaporating body that can be described using (Carslaw & Jaeger 1959)

$$P_i(r_+ = s, t) = RT\frac{s}{D_i}J_{i,\text{net}}[1 - e^{\xi}\,\text{erfc}\,(\sqrt{\xi})] \qquad (A2)$$

where $P_i(r_+ = s, t)$ is the pressure of gas i immediately above the liquid surface, r_+ is the radial distance above the surface of the spherical evaporating body of radius s, D_i is the gas-phase diffusion coefficient for the species i through the ambient gas, and $\xi = tD_i/s^2$ is the dimensionless elapsed time from the start of evaporation.

The isotopic effects of both evaporation and condensation must be included in order to arrive at the net effect of both processes operating simultaneously. The condensation isotope fractionation factor, α_{cond}, is related to the equilibrium and evaporation fractionation factors by the law of mass action:

$$\alpha_{\text{eq}} = \frac{\alpha_{\text{cond}}}{\alpha_{\text{evap}}}. \qquad (A3)$$

Here, α_{eq} is the atomic ratio of heavy-to-light isotopes in the melt divided by that of the vapor at equilibrium, or $(n'_{i,\text{melt}}/n_{i,\text{melt}})/(n'_{i,\text{vapor}}/n_{i,\text{vapor}})$, where the superscript prime signifies the heavy isotope or isotopologue (hereafter "isotope" refers also to isotopologue as appropriate). The evaporation fractionation factor α_{evap} is $(n'_{i,\text{vapor}}/n_{i,\text{vapor}})/(n'_{i,\text{melt}}/n_{i,\text{melt}})$, where the isotope ratio in the numerator is determined by the kinetics of evaporation. Equation (A3) is important because the

return flux of the gaseous heavy isotope to the melt from the vapor is related to that of the light isotopic species by $\alpha_{\rm cond}$. The melt/vapor equilibrium fractionation factor, $\alpha_{\rm eq}$, can be obtained from first principles, and $\alpha_{\rm evap}$ can be obtained from laboratory experiments. However, $\alpha_{\rm cond}$ is less tractable both from theory and from experiments, but it can be calculated using Equation (A3) as $\alpha_{\rm cond} = \alpha_{\rm eq}\,\alpha_{\rm evap}$. The bond energy effect of condensation, a consequence of isotope-dependent vibrational partition function ratios for the vapor and melt, applies to the return flux from the gas phase to the melt such that $J^{*\prime}_{i,{\rm return}} = \alpha_{\rm eq}\alpha_{\rm evap}\,J'_{i,{\rm return}}$, where we use the prime symbol to denote the heavy isotopic species as usual and the star to signify the return flux corrected for the bond energy effects of condensation.

The isotopic fractionation attending condensation comes from comparing the return flux of the light isotopes to the melt,

$$J_{i,{\rm return}} = \frac{\gamma_i P_i}{\sqrt{2\pi m_i RT}}, \qquad (A4)$$

to the return flux of the heavy isotopes to the melt,

$$J^{*\prime}_{i,{\rm return}} = \alpha_{i,{\rm eq}}\alpha_{i,{\rm evap}}\frac{\gamma_i P'_i}{\sqrt{2\pi m'_i RT}}, \qquad (A5)$$

where the vapor pressure of component i directly above the melt is given by Equation (A2). Using Equation (A2), Equation (A4) can be written as

$$J_{i,{\rm return}} = \frac{\gamma_i}{\sqrt{2\pi m_i RT}}RT\frac{s}{D_i}J_{i,{\rm net}}[1 - e^\xi\,{\rm erfc}\,(\sqrt{\xi})] \qquad (A6)$$

and Equation (A5) as

$$J^{*\prime}_{i,{\rm return}} = \alpha_{i,{\rm eq}}\alpha_{i,{\rm evap}}\frac{\gamma_i}{\sqrt{2\pi m'_i RT}}$$
$$\times\ RT\frac{s}{D'_i}J'_{i,{\rm net}}[1 - e^\xi\,{\rm erfc}\,(\sqrt{\xi})]. \qquad (A7)$$

Because the net flux is the difference between the evaporative flux and the return flux, it is straightforward to show that in general

$$\frac{J_{i,{\rm net}}}{J_{i,{\rm evap}}} = \frac{1}{(1 + J_{i,{\rm return}}/J_{i,{\rm net}})}. \qquad (A8)$$

The ratios $J_{i,{\rm return}}/J_{i,{\rm net}}$ for the light isotopes, and similarly $J^{*\prime}_{i,{\rm return}}/J'_{i,{\rm net}}$ for the heavy isotopes, are obtained from Equations (A6) and (A7). With this substitution, Equation (A8) becomes

$$\frac{J_{i,{\rm net}}}{J_{i,{\rm evap}}} = \frac{1}{1 + \frac{\gamma_i RT}{\sqrt{2\pi m_i RT}}\frac{s}{D_i}[1 - e^\xi\,{\rm erfc}\,(\sqrt{\xi})]}, \qquad (A9)$$

and the heavy isotope equivalent is

$$\frac{J^{*\prime}_{i,{\rm net}}}{J'_{i,{\rm evap}}} = \frac{1}{1 + \alpha_{i,{\rm eq}}\alpha_{i,{\rm evap}}\frac{\gamma_i RT}{\sqrt{2\pi m'_i RT}}\frac{s}{D'_i}[1 - e^\xi\,{\rm erfc}\,(\sqrt{\xi})]}. \qquad (A10)$$

The net isotope fractionation factor associated with net evaporation of the two isotopic species is the ratio of the net fluxes of the species relative to the ratio of isotopes in the evaporating melt, such that

$$\alpha_{i,{\rm net}} = \frac{\left(\frac{J^{*\prime}_{i,{\rm net}}}{J_{i,{\rm net}}}\right)}{\left(\frac{n'_{i,{\rm melt}}}{n_{i,{\rm melt}}}\right)}. \qquad (A11)$$

The ratio of net fluxes is obtained from the ratio of Equations (A10) to (A9):

$$\frac{J^{*\prime}_{i,{\rm net}}}{J_{i,{\rm net}}}$$
$$= \frac{J'_{i,{\rm evap}}}{J_{i,{\rm evap}}}\frac{1 + \frac{\gamma_i RT}{\sqrt{2\pi m_i RT}}\frac{s}{D_i}[1 - e^\xi\,{\rm erfc}\,(\sqrt{\xi})]}{1 + \alpha_{i,{\rm eq}}\alpha_{i,{\rm evap}}\frac{\gamma_i RT}{\sqrt{2\pi m'_i RT}}\frac{s}{D'_i}[1 - e^\xi\,{\rm erfc}\,(\sqrt{\xi})]}. \qquad (A12)$$

The ratio of evaporative fluxes on the right-hand side divided by the isotope ratio in the melt is the free evaporation fractionation factor by definition:

$$\alpha_{i,{\rm evap}} = \frac{\left(\frac{J'_{i,{\rm evap}}}{J_{i,{\rm evap}}}\right)}{\left(\frac{n'_{i,{\rm melt}}}{n_{i,{\rm melt}}}\right)}. \qquad (A13)$$

Combining Equations (A11)–(A13) gives an explicit equation for the isotope fractionation factor associated with the net evaporation of species i:

$$\alpha_{i,{\rm net}} = \frac{\left(\frac{J^{*\prime}_{i,{\rm net}}}{J_{i,{\rm net}}}\right)}{\left(\frac{n'_{i,{\rm melt}}}{n_{i,{\rm melt}}}\right)} = \alpha_{i,{\rm evap}}$$
$$\times\ \frac{1 + \frac{\gamma_i RT}{\sqrt{2\pi m_i RT}}\frac{s}{D_i}[1 - e^\xi\,{\rm erfc}\,(\sqrt{\xi})]}{1 + \alpha_{i,{\rm eq}}\alpha_{i,{\rm evap}}\frac{\gamma_i RT}{\sqrt{2\pi m'_i RT}}\frac{s}{D'_i}[1 - e^\xi\,{\rm erfc}\,(\sqrt{\xi})]}. \qquad (A14)$$

This is Equation (7) in the text.

We note that molecular masses both appear explicitly in Equations (A12) and (A14) and also are embedded within the diffusivities D'_i and D_i, and that these masses should both refer to the reduced masses for transport through the gas phase. This is despite the fact that m_i is not often described this way when invoking the Hertz–Knudsen equation; the diffusivities and the return fluxes are affected by the same ratio of reduced masses. This can be seen by evaluating the limit of the net flux ratio given by Equation (A12) where the return flux is high, such that $1 + J_{i,{\rm return}}/J_{i,{\rm net}} \to J_{i,{\rm return}}/J_{i,{\rm net}}$ and where timescales are sufficiently long that $1 - e^\xi\,{\rm erfc}\,(\sqrt{\xi}) \to 1$. In these limits, isotopic equilibrium between the melt and overlying gas should result. Recognizing that $D'_i\big/D_i = \sqrt{\mu_i/\mu'_i}$ where μ_i is the reduced mass for transport through the gas, Equation (A12) as written reduces to

$$\frac{J^{*\prime}_{i,{\rm net}}}{J_{i,{\rm net}}} \sim \left(\frac{n'_{i,{\rm melt}}}{n_{i,{\rm melt}}}\right)\alpha_{i,{\rm evap}}\sqrt{\frac{m'_i}{m_i}}\sqrt{\frac{\mu_i}{\mu'_i}}\frac{1}{\alpha_{i,{\rm eq}}\alpha_{i,{\rm evap}}}. \qquad (A15)$$

This expression is only equal to $(n'_{i,{\rm melt}}/n_{i,{\rm melt}})/\alpha_{i,{\rm eq}}$, as required at equilibrium, if ${\rm m}'_i = \mu'_i$ and $m_i = \mu_i$, showing that the mass effects of transport of the isotopes of species i through

the gas must be the same when evaluating diffusion and the return flux.

Appendix B
Thermal Model for Cooling of the Near-surface LMO

Radiative and conductive cooling of the LMO was modeled using a thermal transport model for a sphere with radius 1700 km. We solved the equation for conductive heat transfer in a sphere at each radial position r_i:

$$\frac{\partial T}{\partial t} = \kappa \left(\frac{\partial^2 T}{\partial r^2} + \frac{2}{r} \frac{\partial T}{\partial r} \right) \tag{B1}$$

where κ is the thermal diffusivity. The initial condition is a body with a uniform temperature of 2800 K. Equation (B1) is solved using explicit finite difference with an outer boundary condition defined by a balance between conductive and radiative heat fluxes at the surface:

$$\kappa \left(\frac{\partial T}{\partial r} \right)_S - \sigma (T_S^4 - T_b^4) = 0, \tag{B2}$$

where T_S and T_b are the surface and ambient background temperatures, respectively, k is the thermal conductivity at the surface, and the partial derivative is evaluated at the surface. In practice, we evaluate the temperature gradient in Equation (B2) using a conductive thermal boundary layer with a scale defined by $(dr)_S = 2\sqrt{\kappa dt}$, where dt is the magnitude of the time step in the numerical scheme and $dT = T_S - T_n$ is the difference in temperatures between the surface and the outermost radial subdivision. This definition of $(dr)_S$ serves as an internally consistent scale for the thermal boundary layer regardless of the presence or absence of convecting melt (see Young et al. 2019). Equation (B2) is solved for the surface temperature using Newton's method at each time step.

We use the substitution $u = rT$ as is usual for spherically symmetric problems and convert Equation (B1) to

$$\frac{\partial u}{\partial t} = \kappa \frac{\partial^2 u}{\partial r^2}. \tag{B3}$$

A central difference formulation is used for the second derivative in Equation (B3) in order to solve for u as a function of t and r. More specifically, we solve Equation (B3) for all locations $n - 1$ in number excluding the outermost subdivision, that is, for $i < n$, using

$$\left(\frac{\partial^2 u}{\partial r^2} \right)_{j+1,i} = \frac{u_{j,i+1} - 2u_{j,i} + u_{j,i-1}}{dr^2} \tag{B4}$$

for time step $j + 1$ and the ith spatial position. The size of the thermal boundary layer is orders of magnitude smaller than the spatial increment dr used throughout the main body (with scales of centimeters versus hundreds of meters, respectively). The central difference approximation, Equation (B4), must therefore be modified for the outermost subdivision of the body to accommodate the unequal spacing between that used in the interior, dr, and that between the outermost subdivision and the boundary layer, $(dr)_S$. We derived the equivalent of Equation (B4) for unequal spacing from the central difference formulations for the first derivatives with different spacings,

yielding for the outermost subdivision $i = n$

$$\left(\frac{\partial^2 u}{\partial r^2} \right)_{j+1,i=n}$$
$$= 4 \frac{(dr)_S u_{j,n-1} - (dr + (dr)_S) u_{j,n} + dr u_{j,S}}{(dr + (dr)_S)(dr^2 + (dr)_S^2)}. \tag{B5}$$

Equation (B5) is similar to the central difference formulation for unequal spacing derived by Singh & Bhadauria (2009) but is more stable for widely different spacings; the limit of Equation (B5) as $(dr)_S \to 0$ is finite, while that for the Singh & Bhadauria simulation is infinity. The difference is how the first derivative evaluated at the nth position is formulated. Here, du/dr at the nth radial position is the average defined by the surface temperature and that at position $n - 1$, while Singh & Bhadauria (2009) use an average weighted by the two distance increments. Both formulations collapse to Equation (B5) where $dr = (dr)_S$, but the weighting in Singh & Bhadauria (2009) leads to numerical instability where $(dr)_S \ll dr$, as in this application.

We included the thermal effects of melting of rock and core formation. Details regarding core formation are found in Zhou et al. (2013). In these models, we assumed that a metallic core forms upon complete melting (our initial condition) with a maximum radius of 300 km. The silicate rock solidus and liquidus are taken from Andrault et al. (2011). The melting reaction progress variable at any given position and time step in the calculations is calculated as

$$f_{\text{sil melt}} = \frac{c_{\text{silicate}}(T - T_{\text{solidus}})}{\Delta H_{\text{sil melt}}} \tag{B6}$$

where c_{silicate} and $\Delta H_{\text{sil melt}}$ are the silicate heat capacity and enthalpy of melting, respectively. Here, complete melting corresponds to $f = 1$, and no melting corresponds to $f = 0$. Equation (B6) accounts for the multivariate (i.e., polythermal at fixed pressure) nature of both rock melting and crystallization from melt.

We simulated convective heat transport by multiplying the conductive thermal diffusivity by the Nusselt number, Nu, in those radial locations where $f_{\text{sil melt}} > 0.9$. The Nusselt number is the ratio of convective to conductive heat transfer in the body and is related to the convective Rayleigh number Ra by $Nu \sim Ra^{1/3}$ (Howard 1966). For these results we used a uniform value for Nu of 10^5. Although larger values are likely applicable, based on estimates of Ra, the value used here adds stability to the solutions where solid and melt are in close proximity. The difference between 10^5 and 10^7, for example, has little effect on the details of the solution near the surface, with the main effect being a smearing of temperature gradients deeper in the body.

The self-consistency of the boundary condition was verified by computing energy balance and ensuring that the system reached a quasi-steady-state energy flux. We verified convergence of the results by first calculating the solutions with greater time and spatial resolution ($dr = 56$ m, $dt = 84$ s) for shorter periods (e.g., 100 yr) and comparing surface temperatures at equivalent elapsed times using larger dr and dt. This comparison permits the identification of the practical limits for dt given a grid spacing dr.
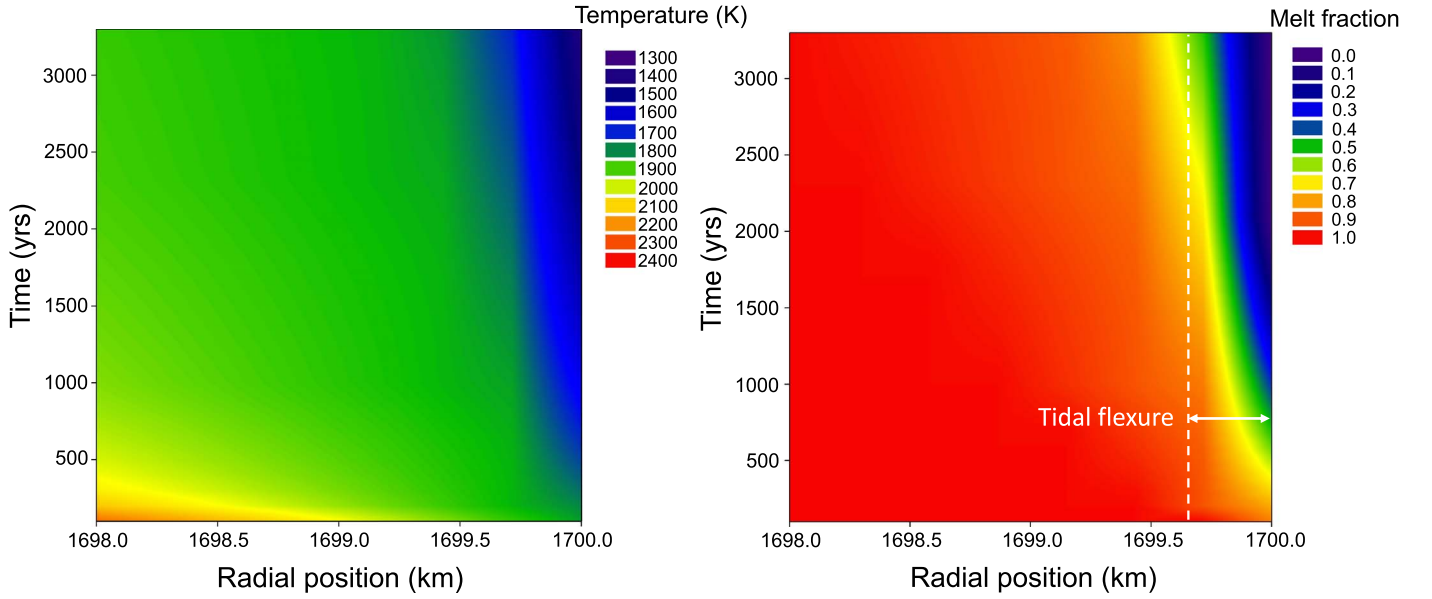
Figure B1. Thermal model showing temperature (left) and melt fraction (right) for cooling of an initially molten Moon with an initial temperature of 2800 K. The abscissa is the radial position relative to the center of the spherically symmetric body. The ordinate is time. Only the outer 2 km of the LMO is shown for clarity. The spatial resolution of this calculation is 283 m. After ∼2000 yr, solidification (melt fraction <0.1) extends to a depth of ∼200 m in this calculation. The magnitude of tidal flexure expected for an orbital eccentricity of 0.01 is shown for comparison.

Figure B1 shows the simulation results. The solidification duration of the surface LMO can be as short as hundreds of years. The surface crust may stay fragile and continuously expose magma to the atmosphere because of the tidal effect from Earth.

Appendix C
Determination of Transonic Point of the Moon for Earth–Moon System

We consider first the transonic point in a spherically symmetric gas atmosphere surrounding an isolated planetary body. In a steady-state atmosphere, conservation of mass and momentum is expressed as

$$\frac{dM_{\mathrm{gas}}}{dt} = 4\pi r^2 \rho \cdot v \tag{C1}$$

and

$$\rho v \frac{dv}{dr} = -\rho \frac{d\phi}{dr} - \frac{dP}{dr}, \tag{C2}$$

respectively, where M_{gas} is the total mass of the atmosphere vapor, v is gas velocity, ρ is gas density, r is the distance from the Moon's center, P is pressure, and ϕ is effective gravitational potential given as $\phi = -GM_p/r$, where M_p denotes the mass of the planetary body and G is the gravitational constant. From Equation (C1) we have

$$\frac{d(\rho r^2 \cdot v)}{dt} = 0, \tag{C3}$$

which can be rewritten as

$$r^2 v \frac{d\rho}{dt} + 2\rho v r \frac{dr}{dt} + \rho r^2 \frac{dv}{dt} = 0. \tag{C4}$$

Dividing by $\rho r^2 v \frac{dr}{dt}$ we obtain

$$\frac{d \ln \rho}{dr} = -\frac{2}{r} dr - \frac{1}{v}\frac{dv}{dr}. \tag{C5}$$

Using the sound speed defined as

$$\frac{dP}{d\rho} = C_s^2 \tag{C6}$$

and an expression for the pressure gradient

$$\frac{dP}{dr} = \frac{dP}{d\rho}\frac{d\rho}{dr} = \rho \frac{dP}{d\rho}\frac{d \ln \rho}{dr} \tag{C7}$$

allows the pressure gradient to be written in terms of the sound speed after substitution of Equations (C5) and (C6) into (C7), resulting in

$$\frac{dP}{dr} = \rho C_s^2\left(-\frac{2}{r} - \frac{1}{v}\frac{dv}{dr}\right). \tag{C8}$$

Combining Equations (C2) and (C8), we then arrive at

$$C_s^2 \frac{2}{r} + C_s^2 \frac{1}{v}\frac{dv}{dr} = \frac{dv}{dr} + \frac{d\phi}{dr} \tag{C9}$$

which can be rearranged to give

$$(C_s^2 - v^2)\frac{dv}{dr} = v\frac{d\phi}{dr} - \frac{2C_s^2}{r}v. \tag{C10}$$

When the gas velocity approaches sound speed, Equation (C10) reduces to

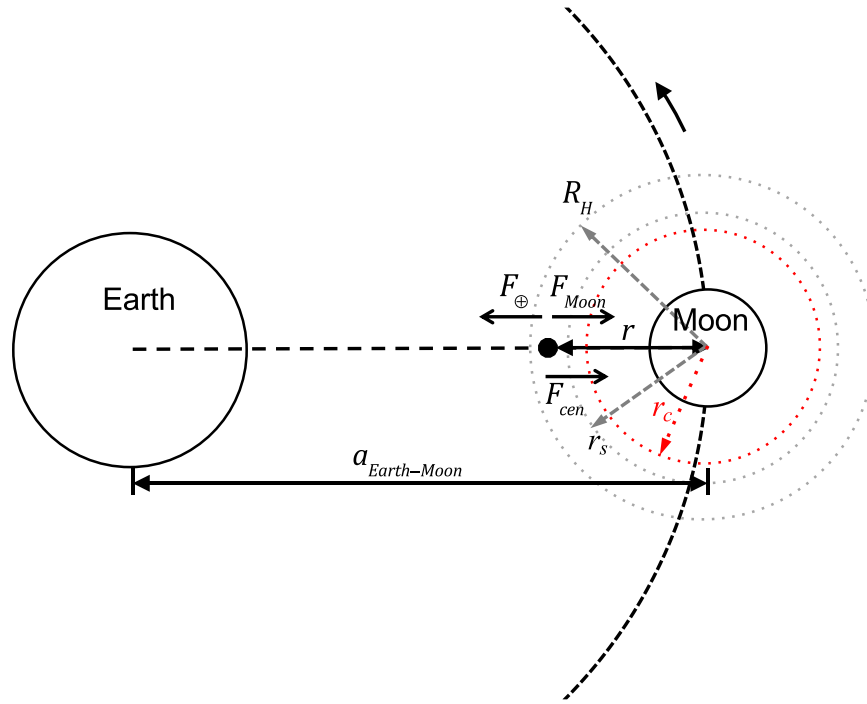$$\left(\frac{d\phi}{dr}\right)_{r=r_s} = \frac{2C_s^2}{r_s}. \tag{C11}$$

Figure C1. Forces considered in the derivation of the transonic radius (r_c) for the Moon, including the influence of the Earth. Here, R_H denotes the Hill radius, and r_s represents the transonic radius from Equation (C12) for the isolated Moon. F_{cen} is the centrifugal force experienced by a molecule, while $F_\oplus$ and F_{Moon} are the gravitational forces due to Earth and Moon, respectively. The diagram is not to scale.

Thus the transonic radius for an isolated planetary body can be determined from the equation

$$r_s = \frac{GM_p}{2C_s^2}. \quad (C12)$$

Next we can consider the transonic radius for the Moon influenced by Earth's gravity in the Earth–Moon system immediately following the Moon's accretion from the giant impact. For convenience we consider two situations: the transonic point located between the Earth and the Moon ($\delta = -1$), and that located at the far side of the Moon ($\delta = +1$). The acceleration of a particle for points located on the line defined by the centers of the Earth and Moon (Figure B1) is

$$\frac{d\phi}{dr} = \frac{GM_{Moon}}{r^2} + \delta \frac{GM_\oplus}{(a + \delta \cdot r)^2} - \delta \frac{GM_\oplus}{a^3}(a + \delta r), \quad (C13)$$

where M_{Moon} and $M_\oplus$ denote the masses of the Moon and Earth, respectively, r is the distance of the point from the center of the Moon, and a represents the Earth–Moon distance. On the right side of Equation (C13), the first and second terms represent the gravitational forces from the Moon and the Earth, and the third term denotes the centrifugal force due to rotation around the Earth. In order to obtain the transonic critical radius (r_c) in this system, we combine Equations (C11) and (C13) where r now refers to the critical radius:

$$\frac{2C_s^2}{r_c} = \frac{GM_{Moon}}{r_c^2} + \delta \frac{GM_\oplus}{(a + \delta \cdot r_c)^2} - \delta \frac{GM_\oplus}{a^3}(a + \delta r_c). \quad (C14)$$

We define the dimensionless parameters $\beta = r_c/R_H$, $\alpha = a/R_H$, and $\theta = R_H/r_s$, where $R_H = a(M_{Moon}/(3M_\oplus))^{\frac{1}{3}}$ is the

Hill radius of the Moon, and $r_s = GM_{Moon}/(2C_s^2)$ denotes the transonic radius of the isolated Moon. Equation (C14) can then be rewritten as

$$\left(\frac{\alpha^3}{3}\right)\beta^5 + (\delta\alpha^4)\beta^4 + (\alpha^5 + \theta\alpha^3)\beta^3$$
$$+ (\delta \cdot 2\theta\alpha^4 - \alpha^3)\beta^2 + (\theta\alpha^5 - \delta \cdot 2\alpha^4)\beta - \alpha^5 = 0. \quad (C15)$$

From here forward we consider the transonic point for the near side of the Moon to illustrate the influence of Earth's gravity on r_c as shown in Figure C1 ($\delta = -1$). Values of β, and thus the critical radii, corresponding to different melt temperatures and Earth–Moon distances can be found from the roots of Equation (C15). The derived critical radii r_c are compared with the Hill radii R_H and the transonic radii r_s in Figure C2. There are two asymptotic values for the derived transonic critical radii: (1) when the Moon is far away from the Earth (high R_H/r_s ratio), the effect from the Earth is negligible and the transonic radius can be calculated from Equation (C12); and (2) when the Moon is close to the Earth (low R_H/r_s ratio), the transonic critical radius is the Hill radius ($r_c = R_H$). Note that the second case occurs only with very short Earth–Moon distances and low temperatures for the Moon (so that r_s is large and thus R_H/r_s is small) and is not achieved in this application. Given the melt temperatures of 1800–2000 K that likely occurred at the surface of the LMO and the likely relevant Earth–Moon distances of 20,000–70,000 km (5.2% to 18.2% of the present Earth–Moon distance), the ratio of r_c/r_s varies from 0.62 to 0.97. As a result, the altitude of the transonic point influenced by Earth's gravity for a Na-dominant rock-vapor atmosphere above the LMO should have varied from ∼500 km
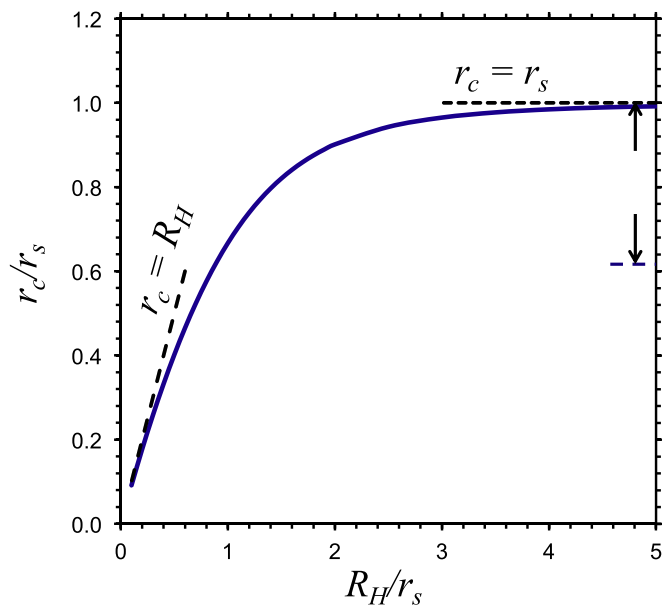
Figure C2. Ratio of the critical point (r_c) determined using Equation (C15) for the lunar rock-vapor atmosphere and the transonic radius (r_s) for an isolated Moon, both as functions of Earth–Moon distance. Earth–Moon distance is expressed as the Hill radius, R_H, relative to the transonic radius. Values for r_c vary with temperature as well. The range shown by the arrows represents the ratio of r_c/r_s corresponding to $T_{LMO} = 1800$–2000 K and $a_{Earth-Moon} \sim$ 20,000–70,000 km (i.e., 5% to 18% of the present Earth–Moon distance). The dashed tangents illustrate that at small Earth–Moon distances with large transonic radii (low atmospheric temperature), the critical radius is equivalent to the Hill radius, while at large Earth–Moon distances with small transonic radii (high atmospheric temperature), the critical radius is equivalent to the transonic radius for an isolated Moon.

up to ∼1800 km above the surface of the Moon. The effects of Earth's gravity as well as Moon's rotation around Earth are to lower the transonic point r_c to inside both the Hill radius (R_H) and the transonic point for the isolated Moon (r_s).

ORCID iDs

H. Tang ⬤ https://orcid.org/0000-0002-9293-3662
E. D. Young ⬤ https://orcid.org/0000-0002-1299-0801

References

Alexander, C. A. O'd. 2001, M&PS, 36, 255
Andrault, D., Bolfank-Casanova, N., Lo Nigro, G., et al. 2011, E&PSL, 304, 251
Armytage, R. M. G., Georg, R. B., Williams, H. M., & Halliday, A. N. 2012, GeCoA, 77, 504
Boyce, J. W., Treiman, A. H., Guan, Y., et al. 2015, SciA, 1, e1500380
Cameron, A. G. W., & Ward, W. R. 1976, LPI, 7, 120
Canup, R. M. 2012, Sci, 338, 1052
Canup, R. M., & Asphaug, E. 2001, Natur, 412, 708
Canup, R. M., Visscher, C., Salmon, J., & Fegley, B., Jr. 2015, NatGe, 8, 918
Carslaw, H. S., & Jaeger, J. C. 1959, Conduction of Heat in Solids (Oxford: Clarendon)
Catling, D. C. 2015, in Treatise on Geophysics, ed. G. Schubert (Oxford: Elsevier), 429, doi:10.1016/b978-0-444-53802-4.00185-8
Ćuk, M., & Stewart, S. T. 2012, Sci, 338, 1047
Davis, A. M., Hashimoto, A., Clayton, R. N., & Mayeda, T. K. 1990, Natur, 347, 655
Day, J. M. D., & Moynier, F. 2014, RSPTA, 372, 20130259
Day, J. M. D., Moynier, F., & Shearer, C. K. 2017, PNAS, 114, 9547
De Pater, I., & Lissauer, J. J. 2006, Planetary Science (Cambridge: Univ. Cambridge Press)
Dhaliwal, J. K., Day, J. M. D., & Moynier, F. 2018, Icar, 300, 249

Elkins-Tanton, L. T. 2008, E&PSL, 271, 181
Fedkin, A. V., Grossman, L., & Ghiorso, M. S. 2006, GeCoA, 70, 206
Floss, C., Goresy, A. E., Zinner, E., et al. 1996, GeCoA, 60, 1975
Freedman, R. S., Marley, M. S., & Lodders, K. 2008, ApJS, 174, 504
Giunta, T., Devauchelle, O., Ader, M., et al. 2017, Geochem. Perspectives Let., 4, 53
Grossman, L., Ebel, D. S., Simon, S. B., et al. 2000, GeCoA, 16, 2879
Grossman, L., Simon, S. B., Rai, V. K., et al. 2008, GeCoA, 72, 3001
Hartmann, W. K., & Davis, D. R. 1975, Icar, 24, 504
Hauri, E. H., Saal, A. E., Rutherford, M. J., & Van Orman, J. A. 2015, E&PSL, 409, 252
Herbort, O., Woitke, P., Helling, C., & Zerkle, A. 2020, A&A, 636, A71
Howard, L. N. 1966, in Proc. XI Int. Congress of Applied Mechanics, ed. H. Görtler (New York: Springer), 1109, doi:10.1007/978-3-662-29364-5_147
Hunten, D. M. 1973, JAtS, 30, 1481
Hunten, D. M., Pepin, R. O., & Walker, J. C. G. 1987, Icar, 69, 532
Kato, C., & Moynier, F. 2017, SciA, 3, e1700571
Kato, C., Moynier, F., Valdes, M. C., Dhaliwal, J. K., & Day, J. M. D. 2015, NatCo, 6, 7617
Knight, K. B., Kita, N. T., Mendybaev, R. A., et al. 2009, GeCoA, 73, 6390
Kruijer, T. S., Kleine, T., Fischer-G. dde, M., & Sprung, P. 2015, Natur, 520, 534
Li, Y., Wang, W., Huang, S., Wang, K., & Wu, Z. 2019, GeCoA, 245, 374
Lock, S. J., Stewart, S. T., Petaev, M. I., et al. 2018, JGRE, 123, 910
Lock, S. J., & Stewart, S. T. 2017, JGRE, 122, 950
Lodders, K. 2003, ApJ, 591, 1220
Longhi, J. 2006, GeCoA, 70, 5919
McCubbin, F. M., & Barnes, J. J. 2019, E&PSL, 526, 115771
Nakajima, M., & Stevenson, D. J. 2018, E&PSL, 487, 117
Nie, N. X., & Dauphas, N. 2019, ApJL, 884, L48
Pahlevan, K., & Stevenson, D. J. 2007, E&PSL, 262, 438
Pahlevan, K., Stevenson, D. J., & Eiler, J. M. 2011, E&PSL, 301, 433
Paniello, R. C., Day, J. M. D., & Moynier, F. 2012, Natur, 490, 376
Parker, E. N. 1964, ApJ, 139, 72
Pierrehumbert, R. T. 2010, Principles of Planetary Climate (Cambridge: Cambridge Univ. Press) doi:10.1017/cbo9780511780783
Pringle, E. A., & Moynier, F. 2017, E&PSL, 473, 62
Richter, F. M. 2004, GeCoA, 23, 4971
Richter, F. M., Davis, A. M., Ebel, D. S., & Hashimoto, A. 2002, GeCoA, 66, 521
Richter, F. M., Janney, P. E., Mendybaev, R. A., Davis, A. M., & Wadhwa, M. 2007, GeCoA, 71, 5544
Roy, A., Wright, J. T., & Sigurdsson, S. 2014, ApJL, 788, L42
Saal, A. E., Hauri, E. H., Van Orman, J. A., & Rutherford, M. J. 2013, Sci, 340, 1317
Saxena, P., Elkins-Tanton, L., Petro, N., & Mandell, A. 2017, E&PSL, 474, 198
Schaefer, L., & Fegley, B., Jr. 2004, EM&P, 95, 413
Sedaghatpour, F., Teng, F.-Z., Liu, Y., Sears, D. W. G., & Taylor, L. A. 2013, GeCoA, 120, 1
Semenov, D., Henning, Th., Helling, Ch., Ilgner, M., & Sedlmayr, E. 2003, A&A, 410, 611
Shahar, A., & Young, E. D. 2007, E&PSL, 257, 497
Sharp, Z. D., Shearer, C. K., McKeegan, K. D., Barnes, J. D., & Wang, Y. Q. 2010, Sci, 329, 1050
Simon, J. I., & DePaolo, D. J. 2010, E&PSL, 289, 457
Simon, J. I., Jordan, M. K., Tappa, M. J., et al. 2017, E&PSL, 472, 277
Singh, A. K., & Bhadauria, B. S. 2009, Int. J. Math. Analysis, 3, 815
Slipski, M., Jakosky, B. M., Benna, M., et al. 2018, JGRE, 123, 2939
Sossi, P. A., Klemme, S., O'Neill, H. S. C., Berndt, J., & Moynier, F. 2019, GeCoA, 260, 204
Sossi, P. A., Moynier, F., & van Zuilen, K. 2018, PNAS, 115, 10920
Stolper, E., & Asimow, P. 2007, AmJS, 307, 1051
Taylor, S. R., Taylor, G. J., & Taylor, L. A. 2006, GeCoA, 70, 5904
Tian, F., & Toon, O. B. 2005, GeoRL, 32, L18201
Touboul, M., Puchtel, I. S., & Walker, R. J. 2015, Natur, 520, 530
Volkov, A. N., Johnson, R. E., Tucker, O. J., & Erwin, J. T. 2011, ApJL, 729, L24
Wang, K., & Jacobsen, S. B. 2016, Natur, 538, 487
Wang, X., Fitoussi, C., Bourdon, B., Fegley, B., & Charnoz, S. 2019, NatGe, 12, 1
Ward, W. R., & Cameron, A. G. W. 1978, LPI, 9, 1205
Wimpenny, J., Borg, L., & Sio, C. 2019, Goldschmidt Abstracts, 2019, 3695
Wood, B. J., & Wade, J. 2013, CoMP, 166, 911
Yamanaka, M. D. 1995, AdSpR, 15, 47
Young, E. D., Kohl, I. E., Warren, P. H., et al. 2016, Sci, 351, 493

Young, E. D., Manning, C. E., Schauble, E. A., et al. 2015, ChGeo, 395, 176

Young, E. D., Nagahara, H., Mysen, B. O., & Audet, D. M. 1998, GeCoA, 18, 3109

Young, E. D., Shahar, A., Nimmo, F., et al. 2019, Icar, 323, 1

Yu, Y., Hewins, R. H., Alexander, C. M. O. D., & Wang, J. 2003, GeCoA, 67, 773

Zahnle, K. J., & Kasting, J. F. 1986, Icar, 68, 462

Zahnle, K. J., Lupu, R., Dobrovolskis, A., & Sleep, N. H. 2015, E&PSL, 427, 74

Zeng, H., Rozsa, V. F., Nie, N. X., et al. 2019, ESC, 3, 2601

Zhang, J., Dauphas, N., Davis, A. M., Leya, I., & Fedkin, A. 2012, NatGe, 5, 251

Zhang, X., & Showman, A. P. 2018, ApJ, 866, 17

Zhou, Q., Yin, Q.-Z., Young, E. D., et al. 2013, GeCoA, 110, 152